UC Irvine

UC Irvine Electronic Theses and Dissertations

Title

Theoretical and Experimental Study on Mass Transfer of Battery Organic Electrolyte in Ambient Air

Permalink

https://escholarship.org/uc/item/9sj064w7

Author

Seo, Bongjin

Publication Date

2021

Peer reviewed|Thesis/dissertation

eScholarship.org Powered by the California Digital Library
University of California

UNIVERSITY OF CALIFORNIA,
IRVINE

Theoretical and Experimental Study on Mass Transfer of Battery Organic Electrolyte in Ambient Air

DISSERTATION

submitted in partial satisfaction of the requirements
for the degree of

DOCTOR OF PHILOSOPHY

in Mechanical and Aerospace Engineering

by

Bongjin Seo

Dissertation Committee:
Professor Yun Wang, Chair
Professor Derek Dunn-Rankin
Professor Jacob Brouwer

2021

© 2021 Bongjin Seo

DEDICATION

To

my parents and friends

who have supported me to finish my journey to Ph.D.

TABLE OF CONTENTS

LIST OF FIGURES

Page

LIST OF TABLES

Page

ACKNOWLEDGEMENTS

My gratitude to committee chair, Professor Yun Wang, who gave me chances to work in his group and to be involved in various experiences. With his guidance, this dissertation would be possible to be written.

In addition, I would like to thank my committee members, Professor Derek Dunn-Rankin and Professor Jacob Brouwer. They were excellent teachers in my classes, committee members in my preliminary exam and qualifying exam. They helped me to pass the exams without a big difficulty, guiding me in a right way for the answers.

My lab members, a former member, Dr. Hao Yuan and present member, Daniela Fernanda Ruiz-Diaz, have been great colleagues and friends. Hao helped me a lot to settle down in my lab and Daniela has been always a great supporter of mine. I would like to express my sincere appreciation to them.

My dear friends, Minji, Gi-Jung, Junyoung, and Jenny reviewed this dissertation to be correctly edited with their passions. With their edits, the quality of this dissertation has been greatly improved.

In addition, I would like to express the deepest appreciation to my family, my parents and sister, and wife, who have supported me with all their hearts. Especially, my wife, Sungyoon, has been with me for all the time during my PhD program, always has stood like a solid column for me to lean against whenever I was suffered.

Bongjin Seo

University of California, Irvine

May 2021

VITA

Bongjin Seo

Department of Mechanical and Aerospace Engineering
University of California, Irvine

Education

2017.9 – 2021.6

Ph.D., Mechanical and Aerospace Engineering, ***University of California, Irvine***, California, USA *(Advisor: Prof. Yun Wang)*

2015.8 – 2016.8

M.Eng., Energy, Environmental and Chemical Engineering, ***Washington University in St. Louis***, Missouri, USA *(Advisor: Prof. Rajan Chakrabarty)*

2013.3 – 2015.2

M.S., Mechanical Engineering, ***Yonsei University***, Seoul, Korea *(Advisor: Prof. Jungho Hwang)*

2005.3 – 2013.2

B.S., Mechanical Engineering, ***Yonsei University***, Seoul, Korea

Publications

1. Zhou, J., **Seo, B.**, Wang, Z., Wang, Y.: Investigation of a Cost-effective Strategy for Polymer Electrolyte Membrane Fuel Cells: High Power Density Operation. *International Journal of Hydrogen Energy*, in review.
2. **Seo, B.**, Wang, Y.: Experimental Measurement of Molecular Diffusion and Evaporation Rate of Battery Organic Electrolytes in Ambient Air. *Journal of the Electrochemical Society*, 2021.
3. Wang, Y**.**, **Seo, B.,** Wang, B., Zamel, N., Jiao, K., Adroher, X. C.: Fundamentals, Materials, and Machine Learning of Polymer Electrolyte Membrane Fuel Cell Technology. *Energy and AI*, 2020.
4. Sumlin, B. J., Oxford, C. R., **Seo, B.**, Pattison, R. R., Williams, B. J., Chakrabarty, R. K.: Density and Homogeneous Internal Composition of Primary Brown Carbon Aerosol. *Environmental Science and Technology*, 2018.
5. **Seo, B. J.**: Flue Gas Purification: Analysis on a Cyclone Separator with CFD and Experiment on a Novel Desulfurization Process. *Master's Thesis*, 2015.

Publications (In Preparation)

1. **Seo, B.**, Hui, X., Wang, Y.: Experimental Testing of Polymer Electrolyte Membrane Electrolysis Cells with Various Solvent Materials in Electrode Preparation. *International Journal of Hydrogen Energy.*
2. **Seo, B.**, Wang, Y.: Investigating the spatial variation of cathode reaction rates in Lithium-air batteries. *Journal of the Electrochemical Society*.

Presentations

1. **Seo, B.**, Oxford, C., Sumlin, B., Pattision, R., Williams, B., Chakrabarty, R.: On the Density and Homogeneous Internal Composition of Brown Carbon Spheres from Biomass Burning. *AAAR Annual Conference*, USA, 2017.
2. **Seo, B. J.**, Jeong, H. J., Hwang, J.: Experiments on Catalyst Influence in Synergy Effect of Coal and Biomass Co-Pyrolysis. *KOSCO SYMPOSIUM*, Korea, 2014.
3. **Seo, B. J.**, Kim, H. J., Kim, C. L., Kim, D. E.: Effect of Temperature on Material Properties of Metals. *KSME Autumn Conference*, Korea, 2012.

Honors and Awards

2017.9 – 2018.6

William & Ida Melucci Space Exploration & Technology Fellowship, Department of Mechanical and Aerospace Engineering, *University of California, Irvine*, California, USA

2013.3 – 2015.2

Four times Full-time Research Assistantship covering all semesters, Department of Mechanical Engineering, *Yonsei University*, Seoul, Korea

2013.9 – 2013.12

Brain Korea 21 Plus Scholarship, Granted by *Korean Government*, Seoul, Korea

2007.9 – 2007.12

Scholarship for the higher GPA, *Yonsei University*, Seoul, Korea

Research Experiences

2017.10 – present

Renewable Energy Resources Laboratory (RERL), Department of Mechanical and Aerospace Engineering, *University of California, Irvine*, California, USA

Research Assistant

• Theoretical and experimental studies on Li-O2 batteries

• Measurement of diffusivities of organic solvents in air for Li-ion batteries

• CFD analysis on mixing-jet of NaI solution in water to quantify concentration profiles.

2016.9 – 2017.5

Aerosol Impacts & Research Lab (AIR), Department of Energy, Environmental and Chemical Engineering, *Washington University in St Louis*, Missouri, USA

Research Scientist

- Measured effective densities of brown carbon aerosol produced from smoldering combustion by using a series of a differential mobility analyzer (DMA) – a centrifugal particle mass analyzer (CPMA) – a condensation particle counter (CPC)
- Measured changes of effective densities of brown carbon aerosol according to thermo-denuding temperatures by using a tandem differential mobility analyzer (TDMA)

2015.12 – 2016.8

Aerosol Impacts & Research Lab (AIR), Department of Energy, Environmental and Chemical Engineering, *Washington University in St Louis*, Missouri, USA

Research Assistant

- Conducted measurement of complex refractive index of brown carbon particles by using an Ellipsometer.
- Measured effective densities of brown carbon particles produced from smoldering combustion by using a series of a differential mobility analyzer (DMA) – a centrifugal particle mass analyzer (CPMA) – a condensation particle counter (CPC)

2013.2 – 2015.3

Nanotechnology, Energy, and Environment Lab, Department of Mechanical Engineering, *Yonsei University*, Seoul, Korea

Research Assistant in Energy Team

- Conducted CFD analysis to optimize flue gas flow in electrostatic precipitators with KC Cottrell Co., Ltd.
  1) Samcheok power plant in Korea
  2) Yeosu combined power plant in Korea
  3) Hatinh power plant in Vietnam
- Researched on characteristics of coal and biomass blend co-pyrolysis using drop tube furnace in Korea Institute of Industrial Technology.
- Conducted CFD study to modify cyclone separators at Yeosu power plant for higher particle-collection efficiency, collaborated with Korea South-East Power Co. and Doosan Heavy Industries and Construction Co.
- Examined chemical kinetics for desulfurization of hydrogen sulfide using liquid tin for advanced high temperature desulfurization process.

2012.6 – 2012.10

Center for Nano-Wear Lab, Department of Mechanical Engineering, *Yonsei University*, Seoul, Korea

Undergraduate Internship

- Researched changes of tribological properties of metals with respect to temperature
- Analyzed coated surface of metal and carbon nanotube using a scanning electron microscope (SEM) and an atomic force microscope (AFM)

Teaching Experiences

2018.9 – 2021.3

Department of Mechanical and Aerospace Engineering, *University of California, Irvine*, California, USA

Teaching Assistant of Introduction to Computer Aided Engineering (MAE 152: 2021 Winter)

Teaching Assistant of Thermal Fluid Science Laboratory (MAE 107: 2018 Fall, 2019, Fall, 2020 Spring, 2020 Fall)

Teaching Assistant of Solar and Renewable Energy Systems (MAE 117: 2019 Winter, 2020 Winter)

Teaching Assistant of Introduction to Thermodynamics (MAE 91, 2019 Spring)

2013.3 – 2014.12

Department of Mechanical Engineering, *Yonsei University*, Seoul, Korea

Teaching Assistant of Thermodynamics

Teaching Assistant of Undergraduate Thesis

Work Experiences

2019.6 – 2019.9

Giner Inc., Boston, USA

Internship for summer (CPT, class of Engr 295)

- Managed and upgraded an electrolyzer test station for high current operation (~180 A)
- Conducted polarization scans and durability tests on proton exchange membrane (PEM) electrolyzer cells.
- Conducted performance tests on anion exchange membrane (AEM) electrolyzer cells.

2016.9 – 2017.5

Washington University in St. Louis, Missouri, USA

Research Scientist, Aerosol Impacts & Research Lab (AIR)

- Details are described in Research Experiences section.

2008.2 – 2010.4

Republic of Korea Air Force, Korea

Soldier, Mechanic for aircraft engines

- Conducted periodic maintenance using endoscope for compressors, combustion chambers, and turbine blades of aircraft engines.
- Repaired and exchanged parts of aircraft engines.
- Tested and operated aircraft engines after repairing and exchanging.

ABSTRACT OF THE DISSERTATION

Theoretical and Experimental Study on Mass Transfer of Battery Organic Electrolyte in Ambient Air

by

Bongjin Seo

Doctor of Philosophy in Mechanical and Aerospace Engineering

University of California, Irvine, 2021

Professor Yun Wang, Chair

A Lithium-ion (Li-ion) batteries are major energy storage resources for electronic devices and electric vehicles. Among the types of Li-ion batteries, the lithium-air (Li-air) battery is promising due to its theoretically high energy capacity which is comparable to that of gasoline. However, formation of lithium oxides from the oxygen reduction reaction (ORR) in the Li-air cathode during discharging operation can cause voltage loss by lithium oxides precipitation in the cathode electrode and eventually leads to a failure of operation. Therefore, understanding the ORR spatial variation is crucial in Li-air cathode design and development. On the other hand, electrolytes are key parts of battery, which provide a pathway for ion transport to the electrochemical reaction sites. Battery electrolyte organic solvents are volatile, flammable, and harmful to the human body, causing eye and skin irritation, soreness, and/or nausea. Battery surface damage in events of electric vehicle collisions or dropping portable devices may cause electrolyte leakage, exposure to air and diffusion in air, raising health concerns. In addition, operation of the Li-air cathodes, which

involves direct contact with ambient air, has a major concern of electrolyte loss if no effective protection layer to prevent electrolyte evaporation is applied.

In the first part of this study, the spatial variation of cathode reaction rates in a Li-air battery was investigated with 1-D reaction-diffusion transfer models for a single- and double-layer cathode structure. In order to find an optimal cathode design with minimum spatial variation, the nondimensionalized equation was analyzed with various *Damköhler* numbers (Da) and transfer coefficients (β) values.

In the second and third parts of this study, evaporation-driven mass transport models were proposed to estimate diffusivity of battery organic solvents in ambient air and the impacts of adding a porous layer. The measured organic solvents are 1,2-dimethoxyethane (DME), dimethyl carbonate (DMC), diethyl carbonate (DEC), and propylene carbonate (PC) which are typical electrolyte materials. After the model of diffusivity in air was validated using liquid water and alcohol, diffusivities of DME, DMC, and DEC are measured and found to be 0.0925 cm^2/s, 0.2116 cm^2/s, and 0.0569 cm^2/s, respectively. The PC testing that showed a liquid loss smaller than the measurement uncertainty due to its slow evaporation rate resulted in failure of measurement. Thus, the proposed method is valid for liquid solvents that have relatively fast evaporation under ambient conditions. The evaporation measurement for the case of a porous layer showed that adding a porous layer effectively depressed solvent evaporation and diffusion. However, the model prediction and the experimental results were inconsistent as they have 1,000 times difference in correction constant (ε^{τ}). One possible hypothesis to account for this large discrepancy is the solubility between the pore material and the liquid solvents.

CHAPTER 1: Introduction

1.1 Motivation and Background

As the global population has been increasing, energy conversion has become a dominant issue [1]. The energy needs of the past, present, and future as shown in Figure 1.1 demonstrate that the energy conversion demands, which was 14 TW in 2014, will likely be doubled by 2050 to continue to meet the worldwide needs [1]. The U. S. Energy Information Administration recently reported that approximately 63% of total energy of the U. S. was produced by converting fossil fuels (e.g., coal and natural gas) in 2017 as shown in Figure 1.2 [2]. Energy conversion from fossil fuel causes the emission of CO_2 which is the dominating source for global warming. To address this problem, several renewable energy sources, such as wind, solar, and biomass have been proposed [1]. However, these sources strongly depend on the facility location and daily-to-seasonal weather dynamics. Large-scale facilities for utilizing renewable energy are dispersed all around the world. To effectively utilize these sources, an efficient energy-storage systems are required. However, the current capacity to store energy from these sources has been reported to be only around 1% [1]. Therefore, it is necessary to develop an alternative technology to store large amounts (magnitude) of energy.

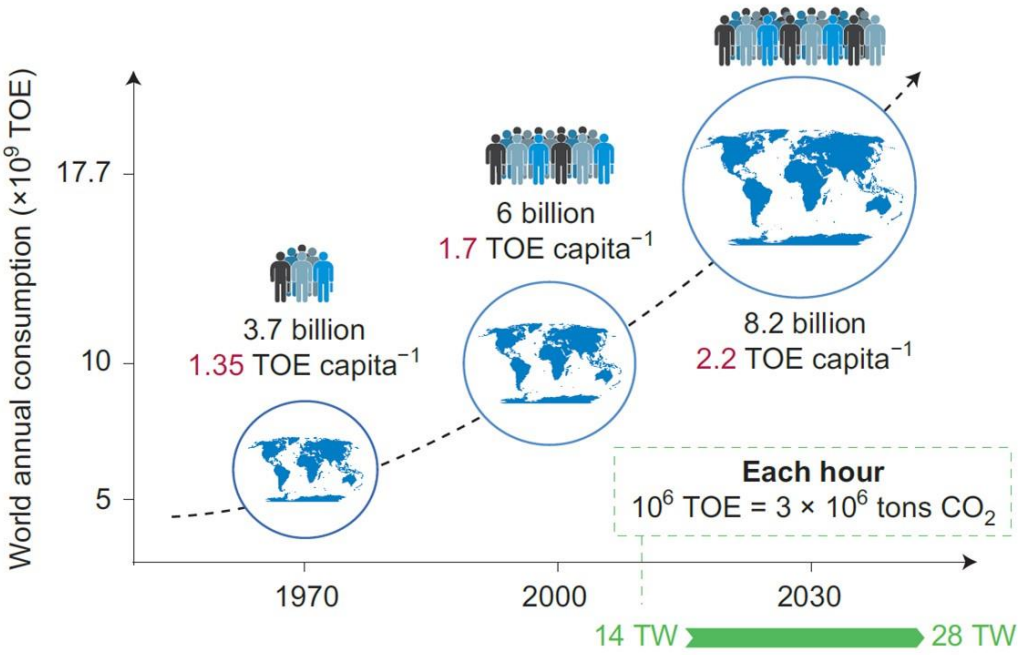

Figure 1.1. Past, present and forecast of the world's energy needs from 1950 to 2050. With the increase in population and changes in lifestyles, the world's energy rate demand is expected to double from 14 TW (2010) to 28 TW (2050). TOE = ton of oil equivalent. Map: © Macmillan Mexico/Haide Ortiz Ortiz, Mario Enrique Ramírez Ruiz [1].

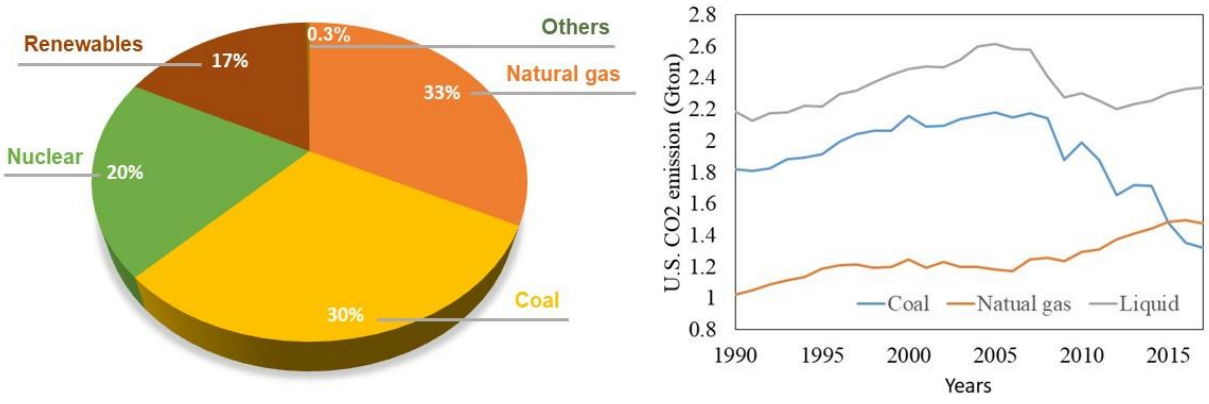

Figure 1.2. (Left) Electricity generation by type in the U.S. (2017). (Right) CO_2 emission by fuel type in the U.S. (2017) [2].

Lithium (Li) based batteries (Li-ion) have been proposed as an alternative energy storage technique due to the unique properties of Li, such as its lightness and low electronegativity (-3.045 V), [3]. A batter's specific capacity to store energy is determined by the capacities of both the cathode and anode materials. Previous research reported that the maximum energy storage in a lithium-graphite battery is 200 mAh/g [3]. Table 1.1 compares the theoretical energy values of energy-storage devices. Even though Li batteries have shown high potential to store energy, their current energy storage capacity is much lower than what is needed to meet the current energy demand.

Table 1.1. Data for several electrochemical reactions that form the basis of energy-storage devices [3].

Battery	Cell voltage (V)	Theoretical specific energy (Wh/kg)	Theoretical energy density (Wh/L)
Li-ion $\frac{1}{2}C_6Li + Li_{0.5}CoO_2 \leftrightarrow 3C + LiCoO_2$	3.8	387	1,015
Zn-air $Zn + \frac{1}{2}O_2 \leftrightarrow ZnO$	1.65	1,086	6,091[a] (ZnO)
Li-S $2Li + S \leftrightarrow Li_2S$	2.2	2,567	2,199[b] (Li+Li_2S)
Li-O_2 (non-aqueous) $2Li + O_2 \leftrightarrow Li_2O_2$	3.0	3,505	3,436[c] (Li+Li_2O_2)
Li-O_2 (aqueous) $2Li + \frac{1}{2}O_2 + H_2O \leftrightarrow 2LiOH$[d]	3.2	3,582	2,234[e] (Li+H_2O+LiOH)

[a]Based on the volume of ZnO at the end of discharge; [b]based on the sum of the volumes of Li at the beginning and Li_2S at the end of discharge; [c]based on the sum of the volumes of Li at the beginning and Li_2O_2 at the end of discharge; [d]assuming the product is anhydrous LiOH and alkaline conditions; and [e]based on the sum of the volumes of Li + H_2O consumed and the LiOH at the end of discharge.

Compared to Li-ion batteries, a lithium-air (or Li-air) battery could be a great promise for high specific energy storage due to its high theoretical energy density [4-7]. Bruce et al. reported a theoretical specific energy of 3,505 Wh/kg for a Li-air battery, which is much larger than that of 387 Wh/kg for a Li-ion battery [3]. In addition, the specific capacity for carbon-based Li-air cathodes was reported as 2500-5000 mAh/g, which is higher than that of Li-ion batteries [8]. Therefore, Li-air battery technique has been extensively investigated since it was first introduced by Abraham and Jiang in 1996 [9]. However, Li-air battery technique has several challenges, such as a slower discharge rate compared to Li-ion battery. In addition, air cathode is one of the most challenging subjects in non-aqueous Li-air battery development [4, 8, 10]. A couple of major problems in the air cathode lead to voltage loss and consequential capacity reduction, such as precipitation of discharge products and electrolyte consumption [4, 8, 11-14]. Precipitates of cathode discharge products in nonaqueous electrolytes are well known to cause voltage loss and eventual shutdown of the discharge operation. Another possible reason for capacity reduction is electrolyte consumption. Since a Li-air battery uses O_2 in air for the cathode, electrolytes are essentially exposed to the ambient air, which is a major difference with other types of batteries. This open structure might result in loss of electrolyte by evaporation. Depletion of electrolytes by electrolyte-consumption prevents Li^+ from transferring from the anode to the cathode, which eventually causes shutting down discharge operation. Therefore, Li oxide precipitation, electrolyte consumption, and slow discharge rate are major issues to be resolved to commercialize Li-air batteries.

In the structure of a battery, an electrolyte is placed in between the anode and cathode electrodes and acts as the media to transport ions between the two electrodes. The type of electrolyte material impacts ion transport, electrochemical reactions (e.g., parasitic reactions), and

spatial variations of electric potentials [15, 16]. Therefore, the selection of electrolyte material is one of the main subjects in battery development. Various compositions of electrolytes have been reported to enhance the performance of electrolytes [17-21]. However, light-metal-based batteries may be damaged, burned, or exploded [17, 18]. In the event of electrolyte leakage from cracks or damage, liquid electrolytes are directly exposed or vaporized to the air, raising health concerns [22-24]. In addition, in metal-air batteries, a redox reaction occurs between the active metal material in the anode electrode and the oxygen in the cathode. The latter is supplied to the cathode structure through ambient air circulation or direct diffusion; thus, electrolyte loss may occur due to evaporation to ambient air, which raises adverse health effect.

A Li-air battery must be open to ambient air as the oxygen reactant at the cathode electrode should be supplied from the air. However, in most cases, an electrolyte is in liquid phase and the liquid has to be maintained inside of the cells while the gaseous reactant needs to be supplied. To resolve this issue, membranes, a porous structure, are installed to selectively allow the gaseous component to enter the cell while the liquid electrolyte stays in the battery cells. In the porous structure, gaseous molecules are transferred by diffusion. However, the diffusive transport would have a different behavior or rate than what might happen in the ambient air due to blockage of the porous structure. Accordingly, the apparent diffusivity would be different (mostly smaller) with the nominal diffusivity even though the gas composition and other conditions, such as temperature and pressure, are the same. In such cases, the corrected coefficient, or effective diffusivity, needs to be determined.

1.2 Research Objectives

Mass transport in advanced energy storage systems is investigated in this dissertation. Chapter 2 focuses diffusive transport and reaction of oxygen reactant of the Li-air battery. In Chapter 3, molecular diffusion of battery organic solvents is measured by using a derived model. In Chapter 4, the model derived in Chapter 3 is further expanded for the diffusion through porous media. The three subjects, along with the detailed objectives, of this dissertation are outlined below. Figure 1.3 demonstrates graphical abstracts of the three subjects.

(1) Investigating the spatial variation of cathode reaction rates in lithium-air battery cathode electrode: To develop a novel advanced multi-layer cathode structure for use in a Li-air battery to improve its capacity, it is important to understand spatial variation of cathode reaction rates. To do so, a theoretical approach to develop the oxygen diffusion and consumption model, including oxygen reduction reaction in the cathode electrode, needs to be conducted. The analytical solution is extended to be useful for multi-layer configurations with minimum spatial variation to reduce the oxygen blockage and voltage loss.

(2) Molecular diffusion and evaporation rate of battery organic electrolytes in ambient air: Battery organic electrolytes are designed to stay inside the cells. However, in events of electric vehicle car crash, battery damage by an unexpected impact, or electrolyte leakage from a battery scratch, the electrolyte can be exposed or evaporated into the air. Organic solvents commonly used as battery electrolytes are known to be harmful to the human body, causing irritation, soreness, and nausea. To understand the behavior of organic solvents in the air, it is crucial to determine evaporation rates and diffusivity of the evaporated organic solvents in ambient air. An evaporation-driven convectional diffusion

model was derived. The model was validated by comparing the results in this study to those reported in the literature.

(3) Evaluation of evaporation and diffusion of gas in porous media: Gas diffusion though porous media occurs in the cathode-air membrane of a Li-air battery. The diffusive transport in porous media behaves differently from the molecular diffusion in air due to the impediment of molecular movements by the structure. With the resistivity idea analogous to thermal resistance of heat transfer, a model was developed to predict the effective diffusivity in porous media The model results were compared to the experimental results.

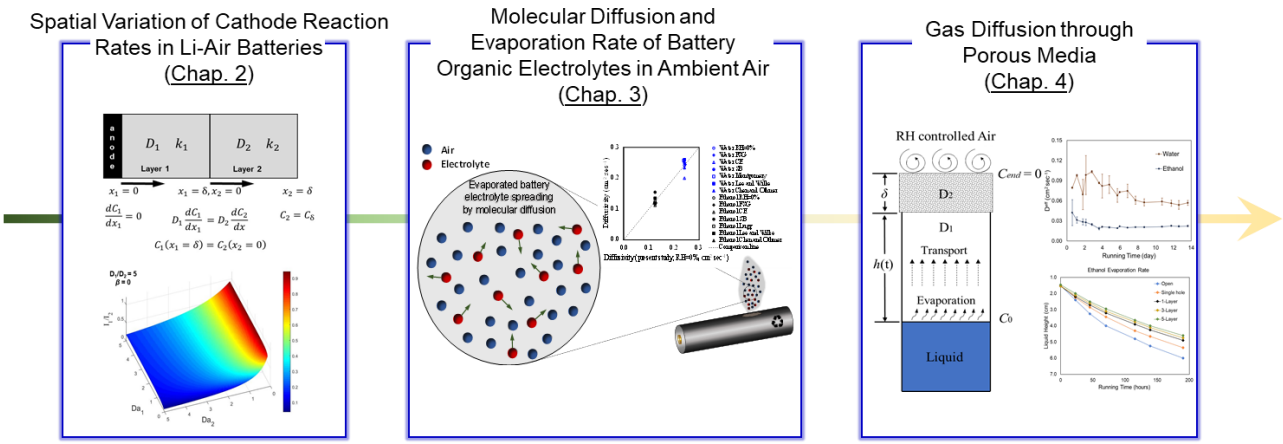

Figure 1.3 Dissertation contents outline.

CHAPTER 2: Spatial Variation of Cathode Reaction Rates in Lithium-Air Batteries

Abstract

In this chapter, spatial variation of cathode reaction rates has been investigated. When oxygen is supplied to the cathode side of Li-Air batteries, oxygen reduction reaction occurs as diffused oxygen reacts with Li^+ to produce power. To investigate the reaction rates, a 1-D transport model has been developed. For the model, a non-dimensionalized transport equation and dimensionless number *Da* have been used to characterize mass transfer while the Tafel equation has been used to model the electrochemical reaction. To verify the developed model for a single layer and multi-layer cathode, the case studies, designed based on literature data of oxygen diffusivity in nonaqueous electrolytes, have been conducted. The single-layer cathode study shows that O_2 concentration at the membrane interface is larger for the smaller *Da* case with any β values. In addition, the larger current value for the smaller *Da* case becomes smaller when dimensionless distance increases over ~0.6. The multi-layer cathode design minimizes the spatial variation of the reaction rates by introducing materials with different diffusivity and reactivity. Large power production due to large reaction rate is not always desirable as it may result in voltage loss by product precipitation in the cathode electrode and consequential oxygen transport blockage. Accordingly, choosing the electrolyte and cathode structure to evenly reduce the reactant concentration is crucial.

2.1 Introduction

Lithium-air battery performance can be predicted by calculating consumption of O_2 in cathode electrode. In discharge operation, the oxygen reduction reaction (ORR) rate determines the production rate of Li oxide precipitates and their volume fraction in cathode at the end of the discharge. The one dimensional (1-D) schematic diagram of a typical Li-air battery and its discharge operation are shown in Figure 2.1.

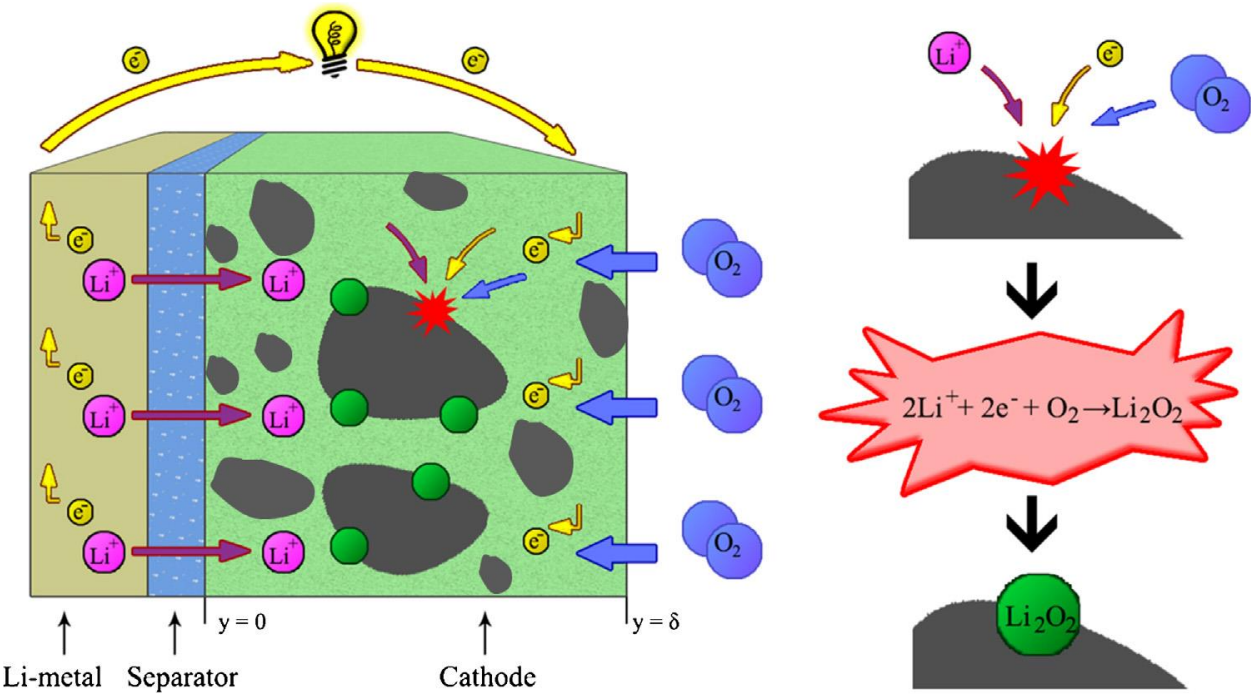

Figure 2.1 Schematic of a Li-air battery and its discharge operation with Li_2O_2 as an example of discharge product. *y* (= *x* in this proposal) starts at the interface between the separator and cathode electrode; and δ denotes the thickness of the cathode electrode [12].

Since magnitude of voltage in the battery depends on the number of remaining pore spaces after precipitation of the discharged products, understanding the ORR spatial variation is significantly important in design and development of the cathode layer for Li-air batteries.

Many studies have been conducted to resolve these issues by exploring electrochemical reaction mechanisms, electrode structures, and materials (e.g., electrolyte and catalyst). Analytical research works have been proposed to indicate the spatial variation of reactant concentrations in consideration of the local ORR rate as well as the effect of the discharge products precipitation in the cathode on the O_2 transport blockage and voltage loss. Wang [11] presented theoretical evaluation on the spatial variations of oxygen, temperature, Li-ion, and phase potentials, and demonstrated that a sufficiently thin cathode would yield a uniform ORR rate across the cathode. Wang and Cho [14] analyzed the spatial variations of major quantities in the cathode, the oxygen concentration profile across the cathode, and the voltage loss caused by the electrode passivation and oxygen transport. They further proposed a 2-D model consisting of conservation of species, charges, and energy to examine spatial variations of the ORR reaction across the cathode and through an oxygen supply channel. The results indicated a large variation in the ORR rate across the cathode, and the variation in the other direction could be significant for thin oxygen supply channels. Wang et al. [12] further explored the spatial variation of oxygen as a function of the Damköhler (*Da*) number and obtained the analytical solutions for the oxygen concentration. In addition, Albertus et al. [25] indicated that precipitate covers the reaction surface in a thin film, resisting electron transport for electrochemical reactions. They proposed a 1-D model following the Li-ion battery approach and predicted spatially varying quantities across the cathode. Williford and Zhang [26] proposed an interconnected dual pore system (one catalyzed and the other non-catalyzed) to improve oxygen transport of the air electrode. The system was analyzed by numerical simulations of finite difference method. Viswanathan et al. [27] investigated the electrical conductivity in Li_2O_2 theoretically and experimentally. They pointed out that the sudden death is related to a critical thickness of Li_2O_2 deposit. Li and Faghri [28] developed a two-dimensional,

transient, and non-isothermal model to investigate on spatial distributions of oxygen, Li-ion, lithium peroxide (Li_2O_2), and temperature in the carbon electrode. They found that thick electrode, the cathode with low open ratio, and high discharge current lowers the utilization portion of the electrode. Andrei et al. [29] presented a model for Li-Air batteries with dual electrolyte using the mass transport and drift-diffusion equations of the electrolyte. They analyzed two regimes of operation: (1) when concentration of the electrolyte is smaller than the concentration of saturation of Li^+OH^- in water; and (2) when the electrolyte concentration is more than saturation concentration, considering deposition of reaction product. They claimed that the limiting factors for low power density of the batteries are the low values of oxygen diffusion coefficient in the cathode and the relatively high separator-anode and separator-cathode interface resistances. Sahapatsombut et al. [30] developed a micro-macro homogeneous mathematical model to determine spatial variation of battery capacity and discharge potential by considering Li_2O_2 layer inside the cathode and active surface morphology changing with the Li_2O_2 growth as well as concentrations of oxygen and Li-ion. Yoo et al. [31] developed a mathematical model in consideration of volume change in Li-Air cell due to metal oxidation in anode and solubility of reaction product in cathode. Their numerical study showed how effective reaction area as well as the volume available for electrolyte changes during operation. They also indicated that the cell voltage cannot be maintained constant because of reduction of the effective reaction area. Sergeev et al. [32] conducted a numerical study to evaluate pore filling at 100% depth of discharge and cell-level specific energy by considering oxygen diffusion and non-uniform product precipitation at different discharge current densities in different electrolytes. Furthermore, Mayur and Bessler [33] proposed a two-dimensional model to investigate a Li-air button cell cathode for five different electrolytes including water, ionic liquid, carbonate, ether, and sulfoxide. They predicted the

spatial distributions of oxygen, Li-ion, and reaction rate in the cathode with respect to electrode saturation. However, little analysis on multi-layer cathode in Li-air battery has been conducted. The multi-layer cathode is more suitable for minimizing radical variation of the cathode reaction rate by tuning the reaction rates with different structures.

In order to improve Li-air battery performance and to understand the mechanisms of Li oxide precipitation, it is significantly important to analyze spatial variation of the cathode reaction rates and Li oxide impact on voltage loss. Based on the analytical results, an optimized double-layer cathode can be designed.

2.2 Theory and Model Development

2.2.1 Spatial Variation of Single-layer Cathode Reaction Rates

The details of ORR in air cathode are described below. Li metal is oxidized in the anode by losing an electron as:

$$\mathrm{Li} \rightarrow \mathrm{Li}^{+} + e^{-} \tag{2.1}$$

The Li^{+} moves to cathode via electrolyte, while the electron moves to the cathode through the outer loop, working as electric current. In the cathode, oxygen gas contained in the air reacts with the Li+ from the Li metal anode as following the reactions below [31],

$$\mathrm{O_2} + e^{-} \rightarrow \mathrm{O_2}^{-} \tag{2.2a}$$

$$\mathrm{O_2}^{-} + \mathrm{Li}^{+} \rightarrow \mathrm{LiO_2} \tag{2.2b}$$

$$2\mathrm{LiO_2} \rightarrow \mathrm{Li_2O_2} + \mathrm{O_2} \tag{2.2c}$$

Therefore, the overall reaction of Li oxide production can be derived from the reaction pathway shown in equation (2.2a-c) as [31],

$$2\mathrm{Li}^{+} + 2e^{-} + \mathrm{O}_2 \rightarrow \mathrm{Li}_2\mathrm{O}_2 \tag{2.3}$$

Oxygen transport is also of importance in calculation of battery performance. In air cathodes, liquid electrolyte is filled with the cathode structure which has a network of pores. The oxygen begins to be dissolved at the electrolyte-air interface, and then the dissolved O_2 is transported to the separator surface by diffusion. However, since the Li+ from anode is transferred to the electrolyte-air interface in the cathode at the same time, O_2 will be consumed by reacting with Li+ to produce the Li oxide precipitates during the species transport. In consideration of the diffusion and reaction, a 1-D transport equation is written as below [34]:

$$\frac{\partial \varepsilon C_{O2}}{\partial t} + \frac{\partial u C_{O2}}{\partial x} = D_{O2}\frac{\partial^2 C_{O2}}{\partial x^2} + \frac{j_c}{nF} \tag{2.4}$$

Considering that the reaction is in steady state and the convectional mass flow is negligible, the 1-D transport equation can be reduced to a simpler form as derived below:

$$D_{O2}\frac{d^2 C_{O2}}{dx^2} = -\frac{j_c}{nF} \tag{2.5}$$

The discharge reaction rate can be approximated expressed by the Tafel equation:

$$j_c = -ai_c = -ai_{0,c}^{ref} C_{O_2}^{1-\beta} C_e^{1-\beta}\, exp\left(-\frac{1-\beta}{RT}F\eta\right) \tag{2.6}$$

where *a* represents the surface-to-volume ratio, determined by the electrode roughness. The surface overpotential η is determined by the local phase potentials and equilibrium potential U_0:

$$\eta = \Phi^{(s)} - \Phi^{(e)} - U_o \tag{2.7}$$

The above considers no precipitates deposited at the reaction surface. For a sufficiently small *Da*, the spatial variations of temperature, phase potentials, oxygen concentration, and C_e are negligibly small; thus, the transfer current density j_c can be treated uniform across the entire thickness of the air cathode. The equation (2.5) can be converted to:

$$D_{O2}\frac{d^2C_{O2}}{dx^2} = kC_{O2}{}^{1-\beta} \quad \text{where } k = \frac{ai_{0,c}^{ref}C_e^{1-\beta}}{nF}\exp\left(-\frac{1-\beta}{RT}F\eta\right) \tag{2.8}$$

In order to solve the equation (2.8), a schematic diagram and boundary conditions drawn in Figure 2.2 are used. Since the concentration of dissolved O_2 can be considered a constant value and O_2 cannot permeate into the separator at the separator-cathode interface, the boundary conditions are determined as below:

$$\frac{dC_{O2}(0)}{dx} = 0 \quad \text{and} \quad C_{O2}(\delta) = C_\delta \tag{2.9}$$

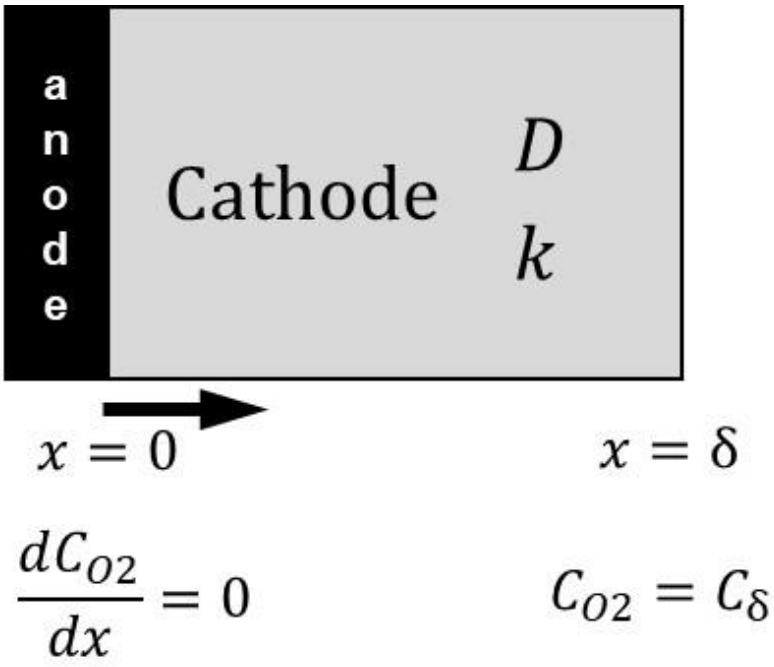

Figure 2.2 Schematic diagram and boundary conditions of single-layer cathode.

To simplify the diffusion equation, let the nondimensionalized concentration and distance set as the following:

$$\overline{C_{O2}} = \frac{C_{O2}}{C_\delta} \quad \text{and} \quad \overline{x} = \frac{x}{\delta} \tag{2.10}$$

The equation (2.8) can be converted to a nondimensionalized form as:

$$\frac{d^2\overline{C_{O2}}}{d\bar{x}^2} = 2Da \cdot \overline{C_{O2}}^{1-\beta} \tag{2.11}$$

Da is the *Damköhler* number, the ratio of reaction rate and mass transport rate, defined as:

$$Da = \frac{k\delta^2}{2D_{O2}{C_\delta}^\beta} = \frac{\text{Reaction rate}}{\text{Mass transport rate}} \tag{2.12}$$

Similarly, the boundary conditions in the equation (2.9) can also be converted to:

$$\frac{d\bar{C}_{O2}(0)}{d\bar{x}} = 0 \quad \text{and} \quad \bar{C}_{O2}(1) = 1 \tag{2.13}$$

For β = 0, a direct solution can be obtained:

$$\overline{C_{O2}} = \frac{\cosh(\sqrt{2Da}\bar{x})}{\cosh(\sqrt{2Da})} \tag{2.14}$$

For β = 0.5, the problem becomes nonlinear, and can be solved by regular perturbation methods for a small *Da*:

$$\overline{C_{O2}} = 1 - Da(1 - \bar{x}^2) + \mathrm{O}(Da^2) \tag{2.15}$$

Combining with the equation (2.6), the equations (2.14) and (2.15) will yield the local reaction rate as:

$$j_c = -ai_{0,c}^{ref} C_\delta C_e \exp\left(-\frac{1}{RT}F\eta\right)\frac{\cosh\left(\sqrt{2Da}\bar{x}\right)}{\cosh\left(\sqrt{2Da}\right)} \quad \text{for } \beta = 0 \tag{2.16}$$

$$j_c = -ai_{0,c}^{ref} \sqrt{C_\delta}\sqrt{C_e} \exp\left(-\frac{0.5}{RT}F\eta\right)\left[1-\frac{1}{2}\left(1-\bar{x}^2\right)Da\right] \quad \text{for } \beta = 0.5 \tag{2.17}$$

For β = 0.5, Taylor series expansion is applied for approximate expression with accuracy O(Da^2). Then, one will obtain the average current density, I, is obtained by integrating j_c from 0 to δ:

$$\mathrm{I} = \int_0^\delta j_c dx = \delta \int_0^1 j_c d\bar{x} = -ai_{0,c}^{ref} C_\delta C_e \exp\left(-\frac{1}{RT}F\eta\right)\frac{\delta\sinh\left(\sqrt{2Da}\right)}{\sqrt{2Da}\cosh\left(\sqrt{2Da}\right)} \quad \text{for } \beta = 0 \tag{2.18}$$

$$\mathrm{I} = -ai_{0,c}^{ref} \sqrt{C_\delta}\sqrt{C_e} \exp\left(-\frac{0.5}{RT}F\eta\right)\left[1-\frac{1}{3}Da\right]\delta \quad \text{for } \beta = 0.5 \tag{2.19}$$

A dimensionless reaction rate can be further defined as below:

$$\frac{\delta j_c}{\mathrm{I}} = \frac{\sqrt{2Da}\cosh\left(\sqrt{2Da}\bar{x}\right)}{\sinh\left(\sqrt{2Da}\right)} \quad \text{for } \beta = 0 \tag{2.20}$$

$$\frac{\delta j_c}{\mathrm{I}} = \frac{1-\frac{1}{2}Da(1-\bar{x}^2)}{1-\frac{1}{3}Da} \quad \text{for } \beta = 0.5 \tag{2.21}$$

2.2.2 Spatial Variation of Multi-layer Cathode Reaction Rates

The single-layer cathode of Li-air battery studied above has several limitations for improving its performance, such as uneven decrease in O_2 concentration followed by uneven Li oxide precipitation in the cathode reaction sites. Therefore, in this section, spatial variation of double-layer cathode reaction rates is studied. Figure 2.3 shows a simple schematic diagram of double-layer cathode and its corresponding boundary conditions. Each cathode layer has different

diffusion coefficients (D_1 and D_2) and reaction rate constants (k_1 and k_2) as well as different 1-D axis (x_1 and x_2). For simplification, it is assumed that the two cathodes have the same thickness (δ). Considering the steady-state reaction and mass transfer as well as negligible convectional mass flow just like in the single-layer cathode case, 1-D transport equations for the two layers can be derived as:

$$D_1 \frac{d^2 C_1}{dx_1^2} = k_1 C_1^{1-\beta} \quad \text{where } 0 \le x_1 \le \delta \tag{2.22a}$$

$$D_2 \frac{d^2 C_2}{dx_2^2} = k_2 C_2^{1-\beta} \quad \text{where } 0 \le x_2 \le \delta \tag{2.22b}$$

The boundary conditions are below,

$$\frac{dC_1(0)}{dx_1} = 0, \;\; C_1(\delta) = C_2(0), \;\; D_1 \frac{dC_1(\delta)}{dx_1} = D_2 \frac{dC_2(0)}{dx}, \;\; C_2(\delta) = C_\delta \tag{2.23}$$

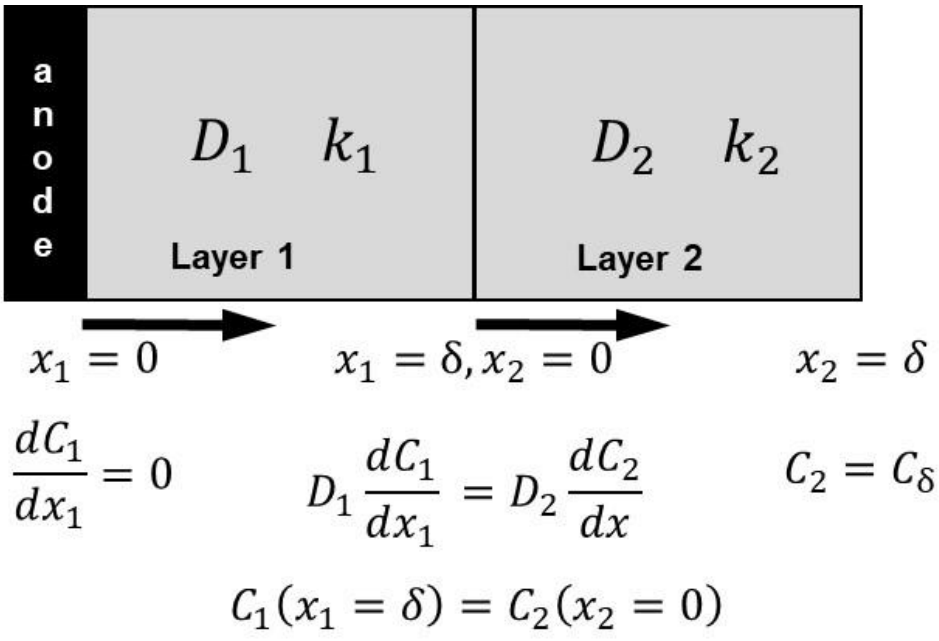

Figure 2.3 Schematic diagram of double-layer cathode and the corresponding boundary conditions.

Similar to the nondimensionalization for single-layer cathode, the equation (2.22a) and (2.22b) are converted to nondimensionalized forms as:

$$\frac{d^2\overline{C_1}}{d\overline{x_1}^2} = Da_1\overline{C_1}^{1-\beta} \quad \text{where } Da_1 = \frac{k_1\delta^2}{D_1 C_\delta^\beta} \tag{2.24a}$$

$$\frac{d^2\overline{C_2}}{d\overline{x_2}^2} = Da_2\overline{C_2}^{1-\beta} \quad \text{where } Da_2 = \frac{k_2\delta^2}{D_2 C_\delta^\beta} \tag{2.24b}$$

For $\beta = 1$, the normalized O_2 concentrations are solved as:

$$\overline{C_1} = \frac{1}{2}Da_1\overline{x_1}^2 - \left(\frac{D_1}{D_2} + \frac{1}{2}\right)Da_1 - \frac{1}{2}Da_2 + 1 \tag{2.25a}$$

$$\overline{C_2} = \frac{1}{2}Da_2\overline{x_2}^2 + \frac{D_1}{D_2}Da_1\overline{x_2} - \frac{D_1}{D_2}Da_1 - \frac{1}{2}Da_2 + 1 \tag{2.25b}$$

For $\beta = 0$, the solutions are below,

$$\overline{C_1} = \frac{D_2\sqrt{Da_2}\cosh\left(\sqrt{Da_1}\overline{x_1}\right)}{D_1\sqrt{Da_1}\sinh\left(\sqrt{Da_1}\right)\sinh\left(\sqrt{Da_2}\right) + D_2\sqrt{Da_2}\cosh\left(\sqrt{Da_1}\right)\cosh\left(\sqrt{Da_2}\right)} \tag{2.26a}$$

$$\overline{C_2} = \frac{D_1\sqrt{Da_1}\sinh\left(\sqrt{Da_1}\right)\sinh\left(\sqrt{Da_2}\overline{x_2}\right) + D_2\sqrt{Da_2}\cosh\left(\sqrt{Da_1}\right)\cosh\left(\sqrt{Da_2}\overline{x_2}\right)}{D_1\sqrt{Da_1}\sinh\left(\sqrt{Da_1}\right)\sinh\left(\sqrt{Da_2}\right) + D_2\sqrt{Da_2}\cosh\left(\sqrt{Da_1}\right)\cosh\left(\sqrt{Da_2}\right)} \tag{2.26b}$$

To obtain the transfer current density, j_c, let us recall the Tafel equation (2.6). The Tafel equation is mainly varied by reaction rate constant, k, as:

$$j_c = nFkC_{O2}^{1-\beta} = nFkC_\delta{}^{1-\beta}\overline{C_{O2}}^{1-\beta} \tag{2.27}$$

where n is the stoichiometric ratio of electron to oxygen, which is assumed to be 2 based on the one-step reaction equation (2.3). The transfer current densities are described as,

$$j_c = nFk_i \quad \text{for } \beta = 1 \tag{2.28}$$

$$j_c = nFk_i C_\delta \overline{C_\iota} \quad \text{for } \beta = 0 \tag{2.29}$$

where *i* represents the layer number. The average current density can be calculated by integrating transfer current densities from 0 to δ.

$$\mathrm{I} = \int_0^\delta j_c dx = \int nFD \frac{d^2 C_{O2}}{dx^2} dx = nFD \frac{dC_{O2}}{dx} = \frac{nFC_\infty}{\delta} D \frac{d\bar{C}}{d\bar{x}} \tag{2.30}$$

Therefore, the average current density for β = 1 can be expressed as:

$$\mathrm{I}_1 = \frac{nFC_\delta}{\delta} D_1 Da_1 \overline{x_1} \tag{2.31a}$$

$$\mathrm{I}_2 = \frac{nFC_\delta}{\delta} [D_2 Da_2 \overline{x_2} + D_1 Da_1] \tag{2.31b}$$

For β = 0, the average current density is expressed as:

$$\mathrm{I}_1 = \frac{nFC_\delta}{\delta} \left[\frac{D_1 D_2 \sqrt{Da_1 Da_2} \sinh\left(\sqrt{Da_1}\overline{x_1}\right)}{D_1 \sqrt{Da_1} \sinh\left(\sqrt{Da_1}\right) \sinh\left(\sqrt{Da_2}\right) + D_2 \sqrt{Da_2} \cosh\left(\sqrt{Da_1}\right) \cosh\left(\sqrt{Da_2}\right)} \right] \tag{2.32a}$$

$$\mathrm{I}_2 = \frac{nFC_\delta D_2 \sqrt{Da_2}}{\delta} \left[\frac{D_1 \sqrt{Da_1} \sinh\left(\sqrt{Da_1}\right) \cosh\left(\sqrt{Da_2}\overline{x_2}\right) + D_2 \sqrt{Da_2} \cosh\left(\sqrt{Da_1}\right) \sinh\left(\sqrt{Da_2}\overline{x_2}\right)}{D_1 \sqrt{Da_1} \sinh\left(\sqrt{Da_1}\right) \sinh\left(\sqrt{Da_2}\right) + D_2 \sqrt{Da_2} \cosh\left(\sqrt{Da_1}\right) \cosh\left(\sqrt{Da_2}\right)} \right] \tag{2.32b}$$

Current density ratio is also crucial in analyzing the Li-air battery performance with the double/multi-layer cathode, which is defined as,

$$\frac{\mathrm{I}_1(\overline{x_1} = 1)}{\mathrm{I}_2(\overline{x_2} = 1)} \tag{2.33}$$

For β = 1, the current density ratio can be expressed as:

$$\frac{\mathrm{I}_1}{\mathrm{I}_2} = \frac{(D_1/D_2)Da_1}{Da_2 + (D_1/D_2)Da_1} \tag{2.34}$$

For $\beta = 0$, the current density ratio is derived as:

$$\frac{\mathrm{I}_1}{\mathrm{I}_2} = \frac{(D_1/D_2)\sqrt{Da_1}\sinh\left(\sqrt{Da_1}\right)}{(D_1/D_2)\sqrt{Da_1}\sinh\left(\sqrt{Da_1}\right)\cosh\left(\sqrt{Da_2}\right) + \sqrt{Da_2}\cosh\left(\sqrt{Da_1}\right)\sinh\left(\sqrt{Da_2}\right)} \tag{2.35}$$

Dimensionless reaction rate for $\beta = 1$ is solved as,

$$\frac{\delta j_{c,1}}{\mathrm{I}_2(\overline{x_2} = 1)} = \frac{\delta^2 k_1}{C_\delta}\left[\frac{1}{D_1 Da_1 + D_2 Da_2}\right] \tag{2.36a}$$

$$\frac{\delta j_{c,2}}{\mathrm{I}_2} = \frac{\delta^2 k_2}{C_\delta}\left[\frac{1}{D_1 Da_1 + D_2 Da_2}\right] \tag{2.36b}$$

For $\beta = 0$, the dimensionless reaction rate is derived below,

$$\frac{\delta j_{c,1}}{\mathrm{I}_2} = \frac{\delta^2 k_1 \cosh\left(\sqrt{Da_1}\overline{x_1}\right)}{D_1\sqrt{Da_1}\sinh\left(\sqrt{Da_1}\right)\cosh\left(\sqrt{Da_2}\right) + D_2\sqrt{Da_2}\cosh\left(\sqrt{Da_1}\right)\sinh\left(\sqrt{Da_2}\right)} \tag{2.37a}$$

$$\frac{\delta j_{c,2}}{\mathrm{I}_2} = \frac{\delta^2 k_2}{D_2\sqrt{Da_2}}\left[\frac{D_1\sqrt{Da_1}\tanh\left(\sqrt{Da_1}\right)\sinh\left(\sqrt{Da_2}\overline{x_2}\right) + D_2\sqrt{Da_2}\cosh\left(\sqrt{Da_2}\overline{x_2}\right)}{D_1\sqrt{Da_1}\tanh\left(\sqrt{Da_1}\right)\cosh\left(\sqrt{Da_2}\right) + D_2\sqrt{Da_2}\sinh\left(\sqrt{Da_2}\right)}\right] \tag{2.37b}$$

A case study was conducted with different diffusion coefficients and reaction rate constants. Then, an analysis on current density ratio with respect to the *Da* numbers and ratio of diffusion coefficients was also conducted. Table 2.1 summarizes the oxygen diffusivity in a few electrolytes. Based on the range of diffusivity in Table 2.1, the conditions for the case study were determined. Reaction constants were set to make *Da* numbers around 1. Table 2.2 shows the conditions for the case study. Case (1) was set as the base and each case has one different value of diffusion coefficient or reaction rate constant. Cases of (2) and (3) have different diffusion

coefficients, and cases of (4) and (5) have different reaction constants. Moreover, each case has two β values (0 and 1), thus, the total number of cases is 10. The *Da* numbers were intentionally adjusted around 0.2~5 for comparisons.

Table 2.1 Oxygen diffusivity in nonaqueous electrolytes [12].

Oxygen diffusivity	Electrolyte	Reference
7.0×10^{-6} cm^2/s	1M $LiPF_6$ in PC:DME (1:1)	[35]
$4.0 – 4.5\times10^{-5}$ cm^2/s	CCl_4	[36]
$5.1 – 5.5\times10^{-5}$ cm^2/s	CS_2	[36]
$2.9 – 3.4\times10^{-5}$ cm^2/s	$C_2H_4CL_2$	[36]
$1.3 – 1.7\times10^{-5}$ cm^2/s	CH_2CL_2	[36]
9.75×10^{-6} cm^2/s	0.1M $TBAPF_6$ in DMSO	[37]
2.45×10^{-5} cm^2/s	0.1M $TBAPF_6$ in MeCN	[37]
1.67×10^{-5} cm^2/s	0.1M $LiPF_6$ in DMSO	[37]
4.64×10^{-6} cm^2/s	0.1 M $LiPF_6$ in MeCN	[37]
1.22×10^{-5} cm^2/s	0.1M $LiPF_6$ in DME	[37]
3.88×10^{-6} cm^2/s	0.1M $TBAPF_6$ in DME	[37]
2.17×10^{-6} cm^2/s	0.1M $LiPF_6$ in TEGDME	[37]
4×10^{-5} cm^2/s	1M Li^+ in DME	[38]
9×10^{-6} cm^2/s	1M Li^+ in PC:DME(1:2)	[38]
2.2×10^{-6} cm^2/s	1M $L:i^+$ in PC	[38]
2.2×10^{-5} cm^2/s	0.1M $TBAClO_4$	[6]
2.1×10^{-5} cm^2/s	0.1M $TBAPF_6$	[6]

Table 2.2 List of reaction constants, diffusion coefficients, and corresponding *Da* numbers for the case study.

Case	1 (base)	2	3	4	5
Thickness [mm]	1.0				
C_δ [m^3/m^3]	0.2				
D_1 [$x10^{-10}$, m^2/s]	1.0	5.0	1.0	1.0	1.0
D_2 [$x10^{-10}$, m^2/s]	1.0	1.0	5.0	1.0	1.0
k_1 [$x10^{-5}$, 1/s]	2.0	2.0	2.0	10.0	2.0
k_2 [$x10^{-5}$, 1/s]	2.0	2.0	2.0	2.0	10.0

Case	β = 0 or 1				
	1	2	3	4	5
Da_1	1.0	0.2	1.0	5.0	1.0
Da_2	1.0	1.0	0.2	1.0	5.0
k_1/k_2	1.0	1.0	1.0	5.0	0.2
D_1/D_2	1.0	5.0	0.2	1.0	1.0
Da_1/Da_2	1.0	0.2	5.0	5.0	0.2

2.3 Results and Discussion

2.3.1 Spatial Variation of Single-layer Cathode Reaction Rates

Figure 2.4. shows spatial variation of nondimensionalized O_2 concentration for (a) $\beta = 0$ and (b) $\beta = 0.5$, respectively. In Figure 2.4(a), for the case of $\beta = 0$, Small *Da* means that the reaction rate is relatively small comparing to its mass transfer rate, thus, less O_2 consumption would occur inside the cathode. As the *Da* increases, the larger the reaction constant is the more O_2 is consumed; therefore, normalized O_2 concentration has more spatial variation. For the case of B=0.5, Figure 2.4(b) has the same overall trend as in Figure 2.4(a); the larger Da causes larger spatial variation of O2 concentration. However, in the case of the same *Da*, while the decreased O_2 concentration for $\beta = 0.5$ is almost similar with that for $\beta = 0$ when $Da = 0.1$ and 0.2, the O_2 concentration0 for $\beta = 0.5$ decreases more than that for $\beta = 0$ when $Da = 0.5$. Moreover, when the exact solution is compared to the approximate solution by the regular perturbation method, the normalized O_2

concentration is the most similar when *Da* = 0.1, and most different when *Da* = 0.5. Such difference can be explained by that the perturbation method assumes a very small *Da*. *Da* = 0.1 or 0.2 can be considered small enough, but *Da* = 0.5 is not small enough to be considered close to 0. This would yield the difference between the approximate and exact solutions. Therefore, the perturbation method is only valid when *Da* number is small enough (e.g. *Da* ~ 0.1).

Figure 2.5 shows spatial variation of dimensionless reaction rate (or dimensionless reaction current) for (a) $\beta = 0$ and for (b) $\beta = 0.5$.The dimensionless reaction rate is a good parameter to understand electric current production in consideration of the cathode thickness.

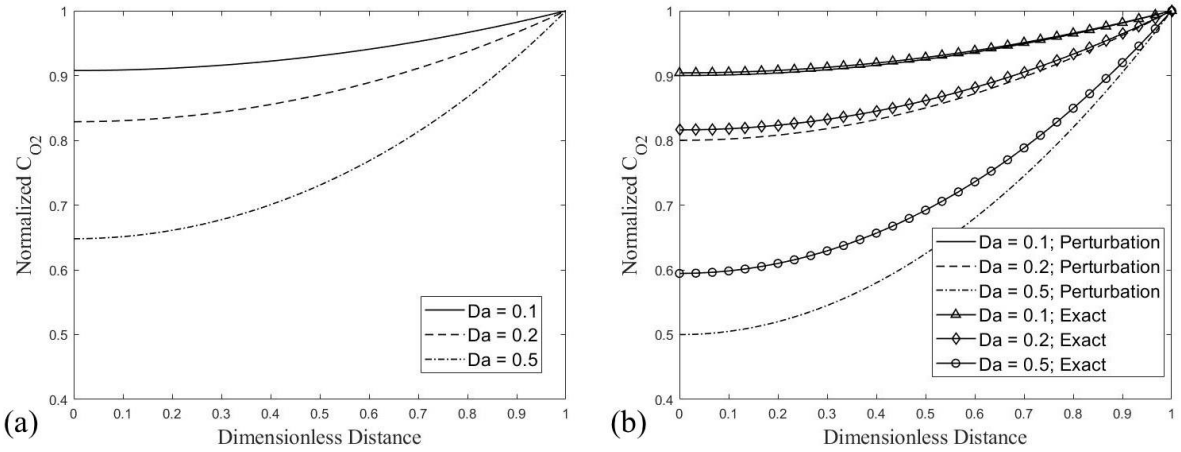

Figure 2.4 Spatial variation of the oxygen content predicted by (a) equation (2.14) for $\beta = 0$ and (b) equation (2.15) and exact solution for $\beta = 0.5$.

In Figure 2.5(a), the dimensionless reaction rate has a larger value when *Da* is larger. Since the cathode thickness is fixed (400 μm in this study), a larger dimensionless reaction rate results from the increase in transfer current density comparted to the increase in electric current density.

This trend is opposite to the trend shown in the normalized O_2 concentration. In Figure 2.5(b), the increasing trend in the dimensionless reaction rate with respect to the large *Da* numbers is the same as for $\beta = 0$. The comparison between exact solution and the approximate solution by perturbation methods and Taylor series expansion show only small difference except for *Da* = 0.5 case.

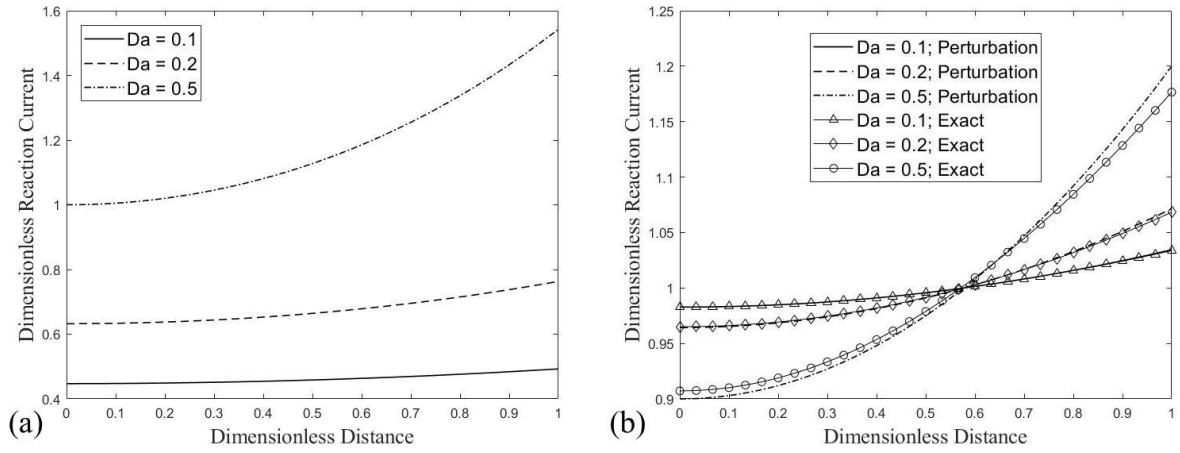

Figure 2.5 Spatial variation of dimensionless reaction rate by (a) equation (2.20) for $\beta = 0$ and (b) equation (2.21) and exact solution for $\beta = 0.5$.

2.3.2 Spatial Variation of Multi-layer Cathode Reaction Rates

Figure 2.6 shows the spatial variation of dimensionless O_2 concentrations with respect to the dimensionless thickness of the double-layer cathode for $\beta = 0$. Considering the case (1) as the baseline, the case (2) that has 5 times larger D_1 than that for the case (1) has a flatter O_2 concentration variation in the first layer and the same O_2 concentration in the second layer. Therefore, only 7.5% of O_2 concentration is consumed, which is smaller than that for case (1) (~9%). For the case (3) which has 5-time larger D_2, the O_2 consumption is only 4%. Even though

large diffusion coefficients facilitate transport of the dissolved O_2 inside the cathode, fast transport prevents from O_2 consumption for electricity production. When considering changes in reaction constants as shown in Figure 2.6b, the case (4) that has 5 times larger k_1 than that of case (1) shows the most amount of O_2 consumption comparing to the cases of (1) and (5). It should be noted that k_1 is the more dominant factor in O_2 consumption than k_2 when comparing the case (4) and (5). For $\beta = 1$ as shown in Figure 2.7, the overall trend is same as that for $\beta = 0$, but the O_2 concentration changes more radically. Specially, case (4) shows all the dissolved O_2 is consumed in the second layer. This is because the ORR is independent from the O_2 concentration for $\beta = 1$.

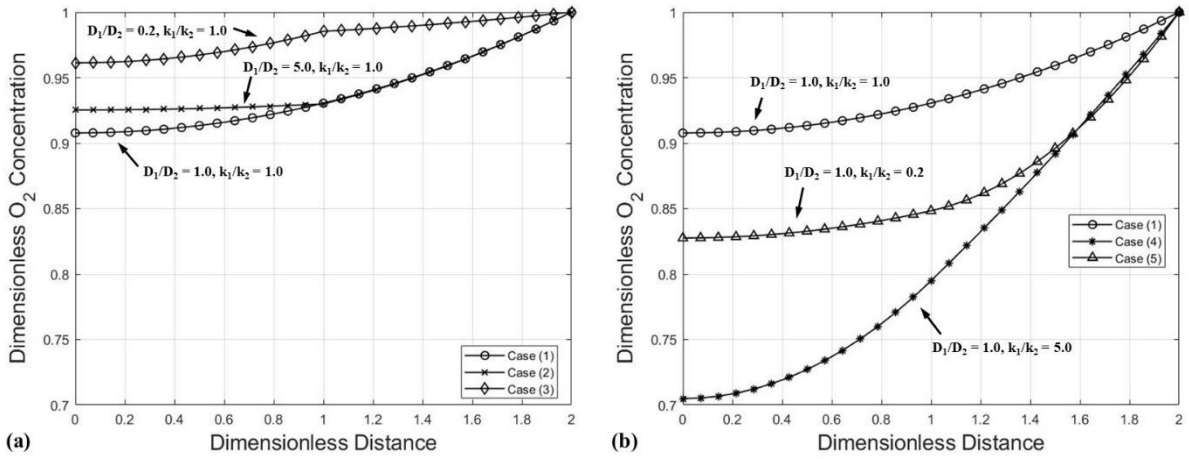

Figure 2.6 Spatial variation of dimensionless O_2 concentration with respect to the dimensionless distance in the double-layer cathode electrode when (a) change in diffusion coefficients ((1), (2), and (3) cases) and (b) change in reaction constants ((1), (4), and (5) cases) for $\beta = 0$.

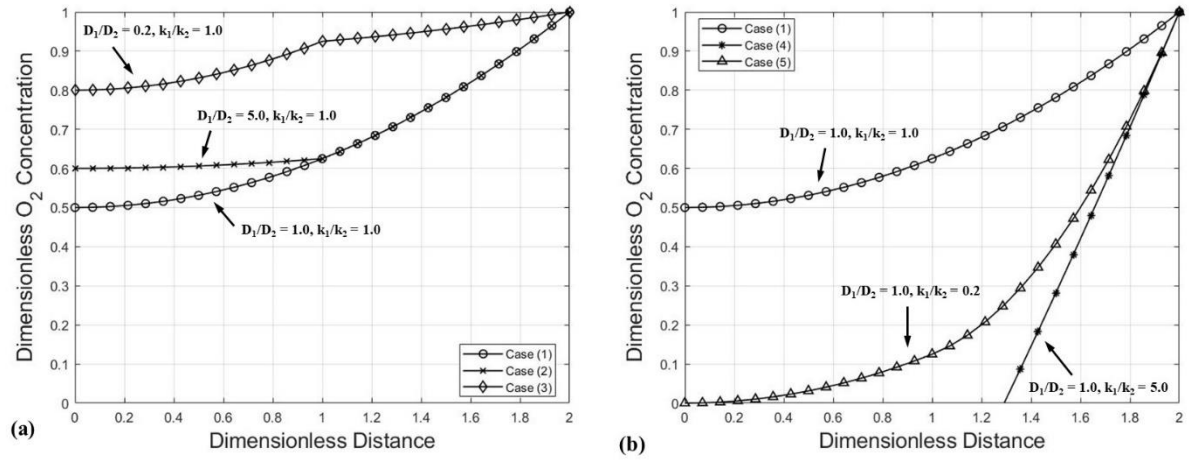

Figure 2.7 Spatial variation of dimensionless O_2 concentration with respect to the dimensionless distance in the double-layer cathode electrode when (a) change in diffusion coefficients ((1), (2), and (3) cases) and (b) change in reaction constants ((1), (4), and (5) cases) for $\beta = 1$.

Figure 2.8 shows the spatial variation of the transfer current density with respect to the dimensionless thickness of the double-layer cathode for $\beta = 0$. Recalling the equation (2.29), the transfer current density depends on the O_2 concentrations and reaction rate constants. Since the changes of O_2 concentration is much smaller than those in the reaction rate constants, the transfer current density mainly varies with the reaction rate constants. Especially, for $\beta = 1$, the transfer current density is a function of reaction rate constants only, which makes the plots in the Figure 2.9 constants.

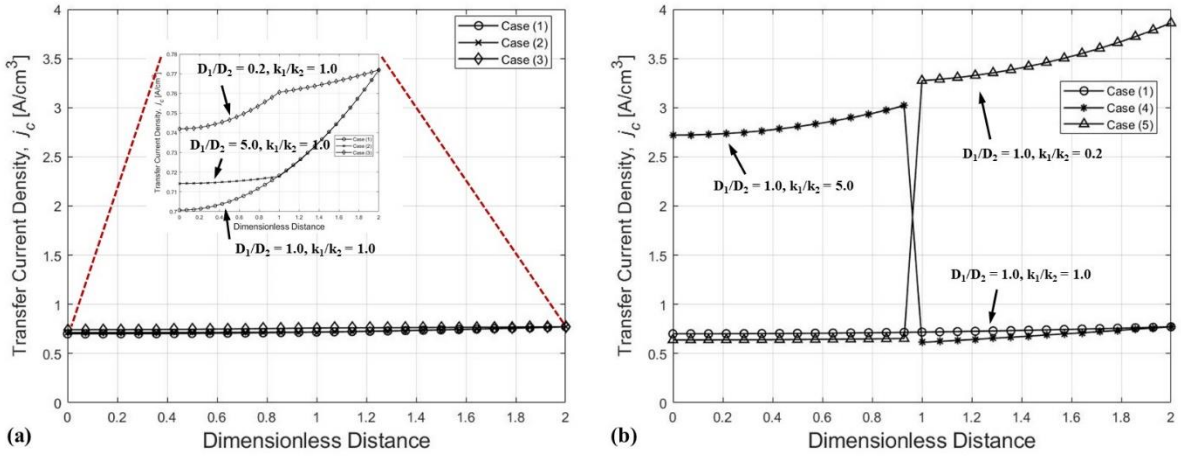

Figure 2.8 Spatial variation of transfer current density with respect to the dimensionless distance in the double-layer cathode electrode when (a) change in diffusion coefficients ((1), (2), and (3) cases) and (b) change in reaction constants ((1), (4), and (5) cases) for $\beta = 0$.

Similarly, the dimensionless reaction rate mainly depends on the transfer current density because the cathode thickness and the electric current density are constant for all the cases. Even though the different electric current density values change the magnitude of dimensionless reaction rate, the overall trend in plots as shown in Figure 2.10 and Figure 2.11 is close to the trend in the transfer current density as seen in the Figure 2.8 and Figure 2.9: The reaction rate constants are the dominant factors for dimensionless reaction rate.

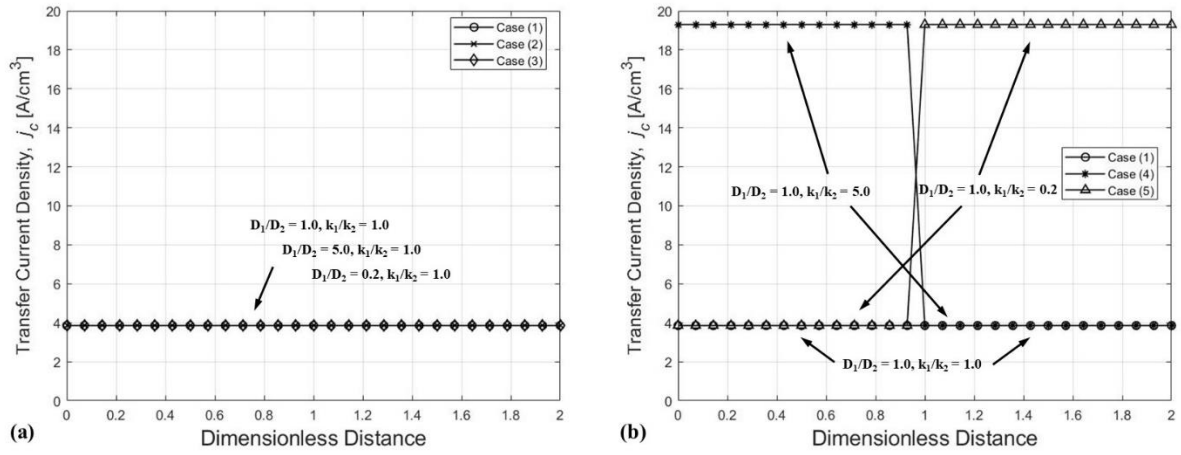

Figure 2.9 Spatial variation of transfer current density with respect to the dimensionless distance in the double-layer cathode electrode when (a) change in diffusion coefficients ((1), (2), and (3) cases) and (b) change in reaction constants ((1), (4), and (5) cases) for $\beta = 1$.

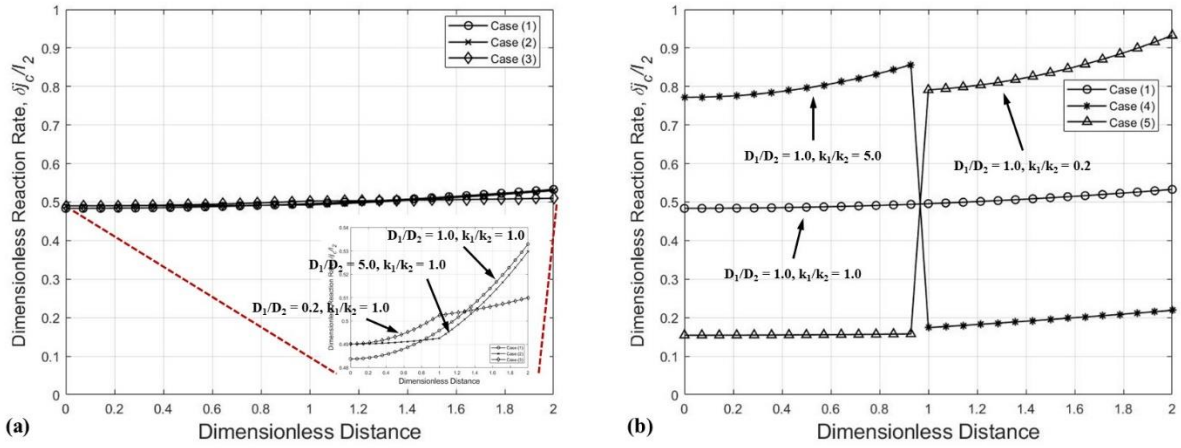

Figure 2.10 Spatial variation of dimensionless reaction rate with respect to the dimensionless distance in the double-layer cathode electrode when (a) change in diffusion coefficients ((1), (2), and (3) cases) and (b) change in reaction constants ((1), (4), and (5) cases) for $\beta = 0$.

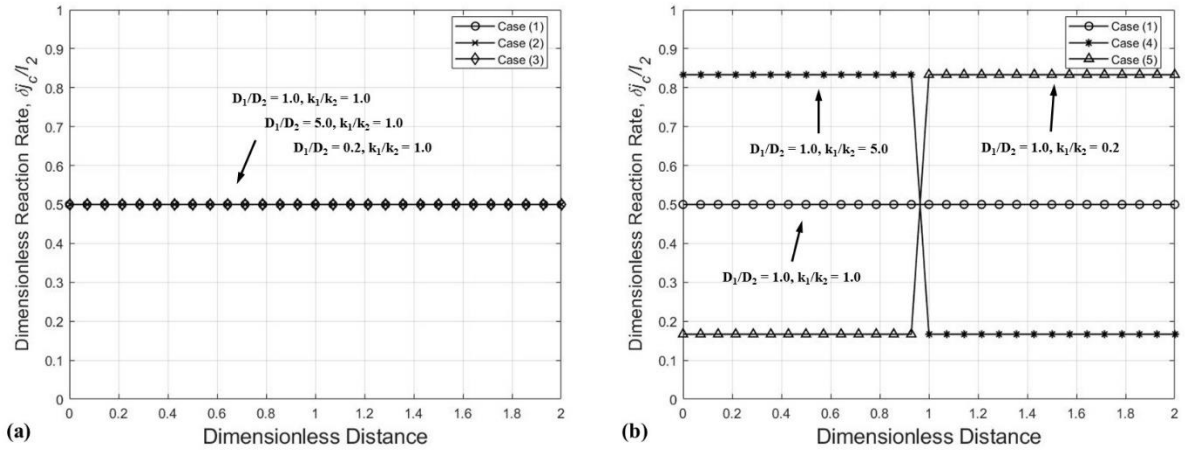

Figure 2.11 Spatial variation of dimensionless reaction rate with respect to the dimensionless distance in the double-layer cathode electrode when (a) change in diffusion coefficients ((1), (2), and (3) cases) and (b) change in reaction constants ((1), (4), and (5) cases) for $\beta = 1$.

Table 2.3 lists the summary of dimensionless O_2 concentration, electric current densities, and current density ratios. It should be noted that the case (4) for $\beta = 1$ has the fastest O_2 consumption, and therefore has the largest electric current density. Moreover, the cases (1)-(3) have similar current density ratios, meaning that reaction rate constant is significant in determining the electric current density.

Table 2.3 Summary of normalized O_2 concentration, electric current densities, and current density ratios.

Case	β = 0				
	1	2	3	4	5
I_1 (x10^{-4} A/m^2)	3.53	3.58	3.74	14.0	3.22
I_2 (x10^{-4} A/m^2)	7.24	7.29	7.57	18.0	21.0
Overall I (x10^{-4} A/m^2)	**10.77**	**10.87**	**11.31**	**32.0**	**24.22**
I_1/I_2	0.49	0.49	0.49	0.78	0.15
$\bar{C}$ $(\bar{x} = 1)$	0.93	0.93	0.99	0.80	0.85
$\bar{C}$ $(\bar{x} = 0)$	0.91	0.93	0.96	0.71	0.83

Case	β = 1				
	1	2	3	4	5
I_1 (x10^{-4} A/m^2)	19.0	19.0	19.0	96.0	19.0
I_2 (x10^{-4} A/m^2)	39.0	39.0	39.0	116.0	116.0
Overall I (x10^{-4} A/m^2)	**58.0**	**58.0**	**58.0**	**212.0**	**135.0**
I_1/I_2	0.49	0.49	0.49	0.83	0.16
$\bar{C}$ $(\bar{x} = 1)$	0.63	0.63	0.93	0.0	0.13
$\bar{C}$ $(\bar{x} = 0)$	0.50	0.60	0.80	0.0	0.0

Figure 2.12 shows a 3-D plot of the electric current density ratios according to Da_1, Da_2 and D_1/D_2. Since there are three independent variables for determining the current density ratio, Da_2 is set up as the x-axis and 4 plots with different Da_1 are drawn in the figure.

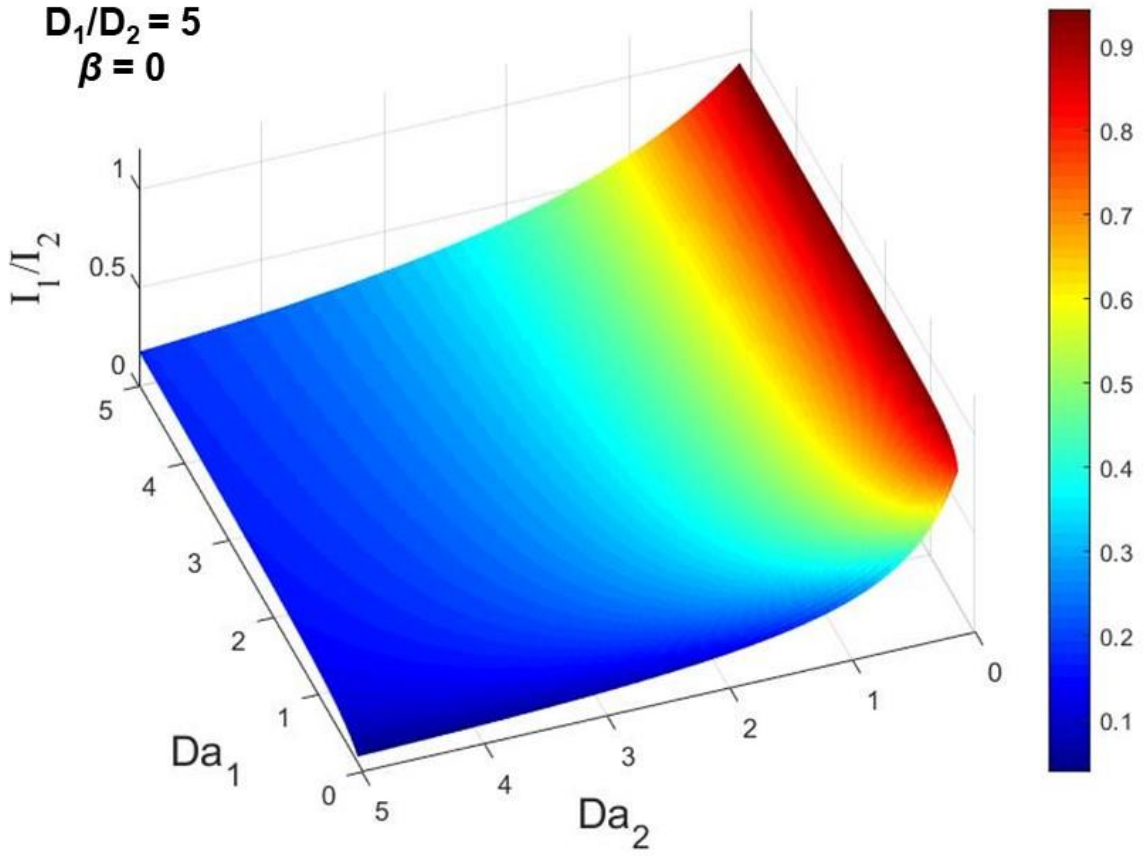

Figure 2.12 Spatial variation of current density ratio with respect to the Da_1 and Da_2 of the double-layer cathode for the case of $D_1/D_2 = 5.0$ for $\beta = 0$ as an example of 3-D plot.

Ideally, the case with electric current density ratio of 0.5 is the best among cases with the same porosity and tortuosity in both layers because the electric current can be evenly produced along with the cathode thickness. Based on the plots in Figure 2.13 and Figure 2.14, various conditions satisfying the electric current density ratio of 0.5 can be found. Furthermore, using the two figures, the battery performance can be adjusted for the desired specification.

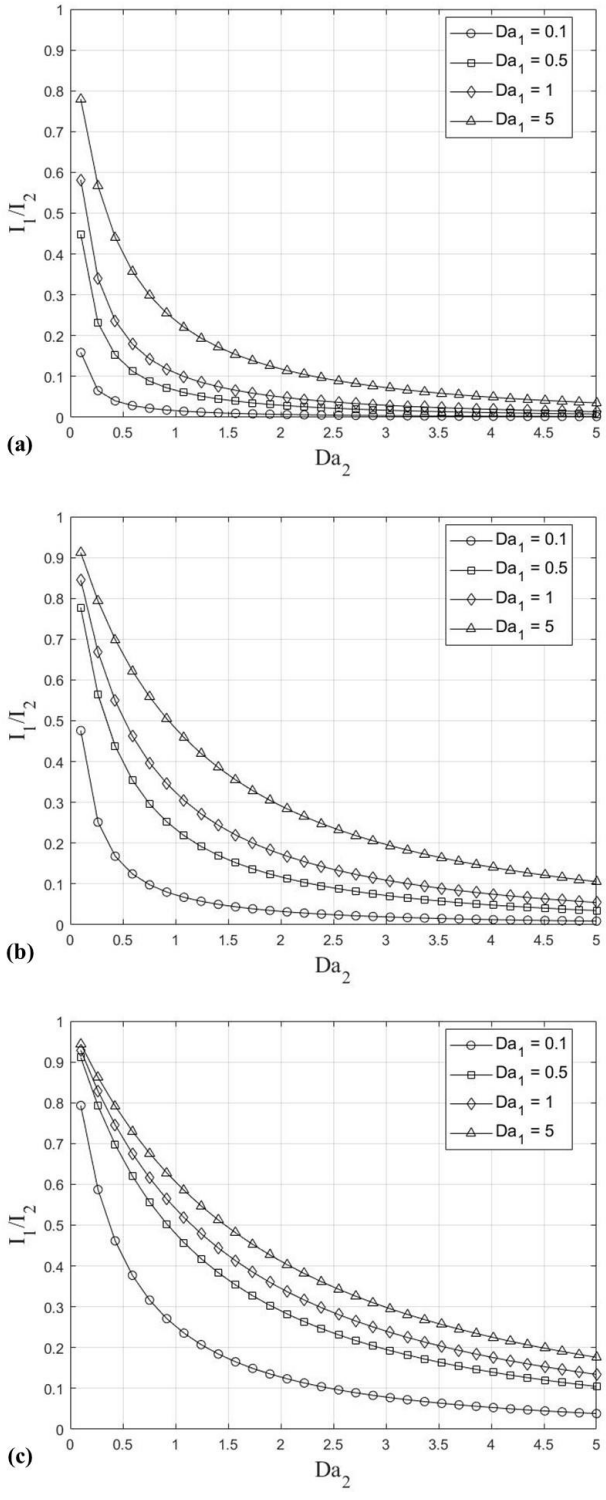

Figure 2.13 Spatial variations of current density ratio with respect to the Da_1 and Da_2 of the double-layer cathode electrode for the cases of D_1/D_2 = (a) 0.2, (b) 1.0, and (c) 5.0 for $\beta = 0$.

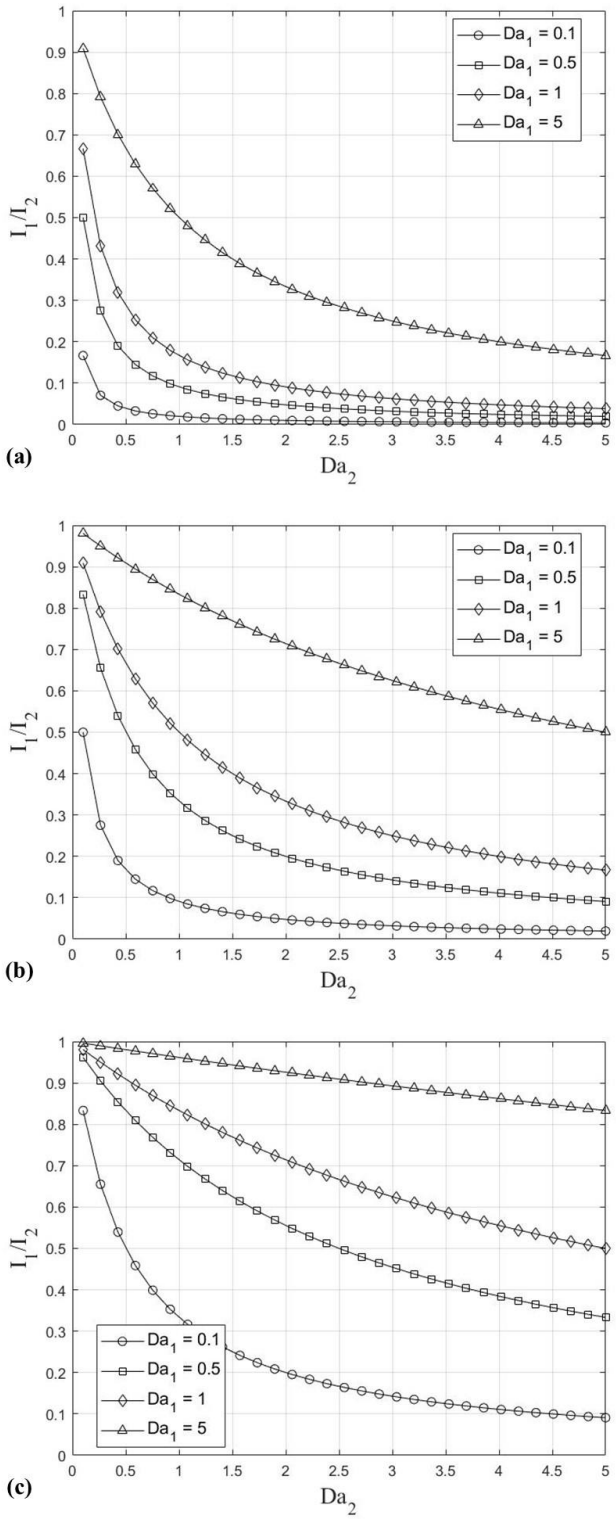

Figure 2.14 Spatial variations of current density ratio with respect to the Da_1 and Da_2 of the double-layer cathode electrode for the cases of D_1/D_2 = (a) 0.2, (b) 1.0, and (c) 5.0 for β = 1.

It should be further studied when the number of layers in a cathode electrode is larger than three, each layer with different thickness. In such cases, finding the oxygen concentration profile would be much more complicated than finding it in the single- or double-layer cases. Modeling multi-layer cathode can start from making a matrix for the double-layer cathode and the matrix can be expanded to the cathodes with multiple layers.

Recalling the equation (2.22a) and (2.22b) and for the case of $\beta = 0$, O_2 concentrations should have forms below,

$$C_1(x) = A_{1,1}\sinh\left(\sqrt{\frac{k_1}{D_1}}x\right) + A_{1,2}\cosh\left(\sqrt{\frac{k_1}{D_1}}x\right) \tag{2.38}$$

$$C_2(x) = A_{2,1}\sinh\left(\sqrt{\frac{k_2}{D_2}}x\right) + A_{2,2}\cosh\left(\sqrt{\frac{k_2}{D_2}}x\right) \tag{2.39}$$

denoting that x is the only 1-D axis starting from 0 to total thickness (d_2) through thickness of the first layer (d_1). A matrix for calculation of O_2 concentration can be derived as below,

$$\begin{bmatrix} \cosh\left(\sqrt{k_1/D_1}\,d_1\right) & -\sinh\left(\sqrt{k_2/D_2}\,d_1\right) & -\cosh\left(\sqrt{k_2/D_2}\,d_1\right) \\ \sqrt{D_1k_1}\sinh\left(\sqrt{k_1/D_1}\,d_1\right) & -\sqrt{D_2k_2}\cosh\left(\sqrt{k_2/D_2}\,d_1\right) & -\sqrt{D_2k_2}\sinh\left(\sqrt{k_2/D_2}\,d_1\right) \\ 0 & \sinh\left(\sqrt{k_2/D_2}\,d_2\right) & \cosh\left(\sqrt{k_2/D_2}\,d_2\right) \end{bmatrix} \begin{bmatrix} A_{1,2} \\ A_{2,1} \\ A_{2,2} \end{bmatrix} = \begin{bmatrix} 0 \\ 0 \\ C_\infty \end{bmatrix} \tag{2.40}$$

Similarly, a 2n-1 by 2n-1 matrix can be derived for n-layers cathode. However, as seen in Figure 2.12, the double-layer cathode has three independent dimensionless variables for electric current density ratio. This means that when one layer is added, more dimensionless parameters

need to be considered, making which will make the analysis and optimization of the multi-layer cathode much complicated.

2.4 Summary

In this chapter, spatial variation of single- and multi-layer cathode reaction rates were investigated. The ORR in air cathode and the major product, Li oxide, were introduced to inform the importance of oxygen distribution in the cathode. Then, a model was derived, starting from 1-D transport equation incorporating diffusion and reaction rates. Tafel equation, an approximation form of Butler-Volmer equation, was chosen to approximately express the reaction. The reaction order was adjusted by using different β values while the transport equation was non-dimensionalized with *Da* not only to simplify but to characterize the diffusion-reaction behavior. After deriving the model for a single layer cathode, a model for multi-layer cathode was further developed to design an optimized combination of the cathode layer with the minimal spatial variation of the reaction rates.

In addition to development of the models, a set of case studies was conducted with different diffusion coefficients and reaction rate constants. In the single-layer cathode study, the results showed that smaller *Da* case results in less consumption of O_2, so that the O_2 concentration at the membrane surface will be larger for any β values. On the other hand, dimensionless reaction current varied with different β values. For $\beta = 0$ case, the dimensionless reaction current is smaller when *Da* was smaller while for $\beta = 0.5$ case, there was a cross-point that the dimensionless reaction current of smaller *Da* case becomes larger which is around 0.6 of dimensionless distance. However, under a certain distance, the current value of the smaller *Da* is larger. In the multi-layer cases studies, it was possible to avoid rapid change in O_2 concentration reduction by manipulating ratios of diffusivity and reactivity. Even though a rapid reduction of O_2

concentration due to a large reaction constant enabled large power generation, it may result in voltage loss by product precipitation in the cathode electrode and consequential oxygen transport blockage. Accordingly, selecting the right electrolyte and cathode structure to evenly reduce the reactant concentration was a key point in multi-layer design. Spatial variation of current density regarding both D_1 and D_2 were determined in 3-D plots which would be helpful in designing double-layer cathode for Li-air battery. Lastly, a general matrix form solution for multi-layer cathode case was introduced.

CHAPTER 3: Molecular Diffusion and Evaporation Rate of Battery Organic Electrolytes in Ambient Air

The contents in this chapter have been published to Journal of Electrochemical Society (Title: Experimental Measurement of Molecular Diffusion and Evaporation Rate of Battery Organic Electrolytes in Ambient Air) in 2021.

Abstract

In this Chapter, I measured the molecular diffusivity and evaporation rate of organic solvents - 1,2-dimethoxyethane (DME), dimethyl carbonate (DMC), diethyl carbonate (DEC), and propylene carbonate (PC) - in ambient air, which are commonly used in light metal batteries, such as Li-ion, Li-air, and Na-O_2 batteries. The measurement was conducted through evolution of the evaporation rate of a liquid solvent in a glass tube, which was designed based on a one-dimensional (1-D) mass transfer model. The experiment successfully measured the diffusion coefficients of DME (0.0925 cm^2/s), DMC (0.2116 cm^2/s), and DEC (0.0569 cm^2/s) in dry air, but failed for that of PC. The PC testing showed a liquid loss smaller than the measurement uncertainty due to its slow evaporation rate under the experimental condition. In the ambient air with the relative humidity (RH) of 50±5%, higher water-soluble solvents showed more reduction in diffusivity calculation compared to that under the dry condition, which is likely due to uncertainty arising from water dissolving to the testing liquid. In addition, I also investigated the time constant for experimental measurement. For the organic liquids, the effective running time can be up to 10 days at room temperature.

3.1 Introduction

Battery technology has been considered as a major energy storage method for renewable energy due to its high energy efficiency, modularity, and pollution-free operation [39]. Lithium-ion (Li-ion) battery is widely used because of its light weight, fast chargeability, excellent durability, and high energy density that mainly ranges 120-300 Wh/kg [40, 41]. In addition, new types of batteries, such as lithium-sulfur (Li-S), lithium-oxygen (Li-O_2) [42], and zinc-oxygen (Zn-O_2), have been recently developed and investigated [3, 43]. The structure of a typical battery is depicted in Figure 3.1. As seen in the figure, an electrolyte is placed between the anode and cathode electrodes and acts as a medium to transport ions between the two electrodes. The type of electrolyte material impacts ion transport, electrochemical reactions (e.g., parasitic reactions), and spatial variations of electric potentials [15, 16]. Therefore, electrolyte selection is one of the main subjects in battery development.

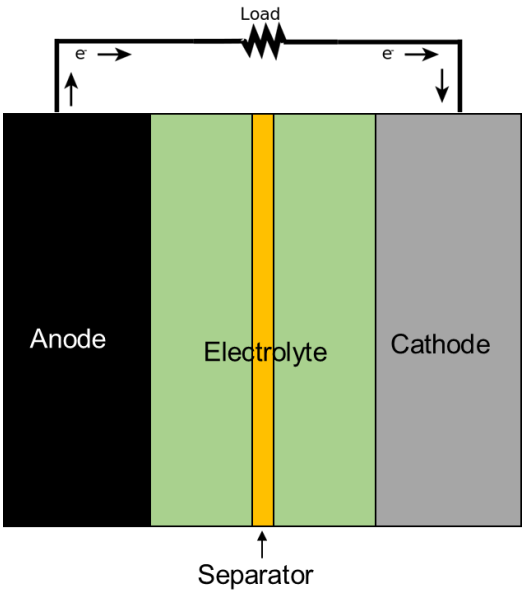

Figure 3.1 Typical battery structure.

One main type of battery electrolytes is aqueous electrolytes, which are extensively used in many conventional batteries, such as alkaline battery, lead-acid battery, and nickel-metal hydride battery [44-47]. Due to substantially negative couple voltage of light metal (Li/Li^+), light-metal/air batteries have intense reactions with water, resulting in safety issues with using aqueous electrolytes in such types of batteries [43]. Nonaqueous electrolytes are another main type of electrolyte for batteries, such as 1,2-dimethoxyethane (DME) [16-18], dimethyl carbonate (DMC) [17-19, 48], diethyl carbonate (DEC) [18-20, 48], and propylene carbonate (PC) [18, 19, 49], which can effectively resolve this issue. In most cases, their mixtures of various composition ratios are employed to enhance the performance of electrolytes [17-21]. Even though intense reactions between Li and water can be prevented by using nonaqueous electrolytes, light-metal-based batteries may be damaged, burned, or exploded [17, 18], e.g. electric vehicles catching fires when the lithium-ion battery is damaged from car accidents. Figure 3.2 demonstrates a conceptual schematic diagram of evaporation and diffusion of the organic electroyte. As seen on the right side of the figure, when electrolyte leakage occurs from various damages, the liquid electrolytes are directly exposed or vaporized into the air, which raises health issues [22-24]. In addition, in metal-air batteries, as shown on the left side of Figure 3.2, a redox reaction occurs between the active metal material in the anode electrode and the oxygen in the cathode. The latter is supplied to the cathode structure through ambient air circulation or direct diffusion, thus electrolyte loss may occur due to evaporation to ambient air and spread by diffusion, which also raises adverse health health effects. Diffusion is a type of mass transfer, where molecules from an area of higher concentration move to an area of lower concentration. It should be noted that the movement of each molecule is randomized, however, the direction of movement statistically follows the concentaration gradient. Organic solvents have been reported to have harmful effects on the human

body. For instance, DME has reproductive toxicity, DEC and DMC cause eye and respiratory irritation, and PC can also cause eye irritation [50-53]. It was also reported that exposure to industrial solvents, usually hydrocarbon compounds, may induce vertigo and nausea [54]. Organic solvents have also been reported to adversely affect human health, such as hearing health, by inpacting the central auditory pathways [55-57]. Thus, it is important to evaluate the evaporation rate of organic solvents in ambient air. In indoor environments (e.g. airplanes, cars, and offices), such leakage or evaporation of organic electrolytes into surrounding air will cause more severe health effects. In addition to evaporation, molecular diffusion also plays an important role in electrolyte vapor transport in ambient air. In this study, the diffusion and evaporation rates of battery organic solvents in ambient air are experimentally investigated.

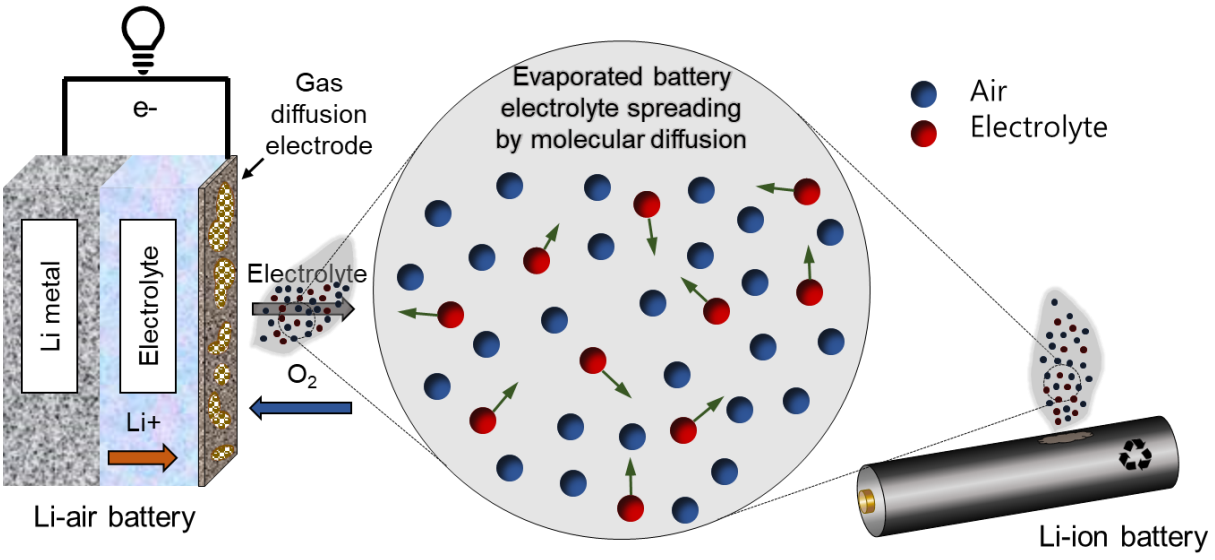

Figure 3.2 A conceptual schematic diagram of evaporation and diffusion of battery organic electrolyte.

To date, several measurement methods have been proposed to experimentally determine gaseous diffusion coefficients. Cowie and Watts [58] used infrared (IR) spectrophotometry to determine the gas concentrations in a diffusion cell by scanning its absorption band. Pommersheim and Ranck [59] used the Stefan cell to measure the interface depth with the corresponding time. Then, a solution using a quasi-steady-state analysis was derived to find the gas diffusion coefficients. Guo et al. [60] used a holographic interferometric system that permits to observe interference fringe by the concentration changes of DMC in heptane and in the air at 5-65 °C. They also derived an equation based on Fick's law of 1-D diffusion to calculate diffusion coefficients using their experimental data. Funazukuri et al. [61] used the Taylor dispersion measurement, which employs photo spectroscopy to measure the concentration profile of a gas species along a pipe flow to determine binary diffusion coefficients of acetone in carbon dioxide. They derived an equation to determine the concentrations at the pipe exit from a convection-diffusion model. Sun et al. [62] developed a new method to measure liquid diffusivity by using changes in the refractive index, which takes a much shorter time than traditional methods. They made asymmetric liquid-core cylindrical lens (ALCL) for 1-D flow and imaging process.

Although attempts have been made to measure the diffusivity of gas species, only a few studies have been proposed to experimentally measure the diffusivities of DME, DMC, DEC, and PC in ambient air. Providing that batteries are now playing an important role in electric vehicles, cell phones, and laptops, it is important to assess their transport and evaporation behaviors in the ambient and evaluate the impacts on human health upon leakage. In this work, the diffusivity and evaporation rates of major organic solvents in ambient air for Li-ion and metal-air batteries were experimentally investigated. In order to determine the diffusivity, we derived a formula based on the Stefan's evaporation-transport (diffusion) model. The model was also validated by comparing

our experimental data of water and ethanol with those from the literature. The impact of RH in the ambient was investigated, and the time constant was analyzed.

3.2 Theory and Experiment

3.2.1 Theory

In the experiment, the evaporation-driven convection-diffusion model [63] is used to calculate diffusion coefficients. Evaporation of liquid electrolyte in a vertical glass tube exposed to ambient air is assumed as a 1-D transport problem, as shown in Figure 3.3. The vertical glass tube, with a specific radius (*R*) and height (*H*), is open to the air and is initially filled with an electrolyte. Assuming air is a type of pure gas, air and electrolyte vapor can be treated as a binary gas mixture. If the pseudo-steady analysis is valid, the mass balance equation can be developed using Fick's law as:

$$N_{BZ} = x_B(N_{AZ} + N_{BZ}) - C_g D_{AB} \frac{dx_B}{dz}, \tag{3.1}$$

where *A* and *B* represent air and electrolyte, respectively, and *N*, C_g, *D*, *x*, *z* are denoted as the molar flux of species, molar concentration of gaseous species, diffusion coefficient, molar fraction, and the axial direction, respectively. For slow evaporation, the liquid-gas interface can be assumed to be stationary, which simplifies equation (3.1) as,

$$N_{BZ}(x_B - 1) = C_g D_{AB} \frac{dx_B}{dz}. \tag{3.2}$$

By integrating both sides, the molar flux of *B* according to time (*t*) is obtained as,

$$N_{BZ}(t) = -\frac{C_g D_{AB}}{h(t)} ln\left(\frac{1-x_0}{1-x_h}\right), \tag{3.3}$$

where $h(t)$, x_0 and x_h represent the solvent height with respect to time, the molar fraction of vaporized solvent at the liquid-air interface, and the molar fraction of the vaporized solvent at the top of the glass tube, respectively. Because of no heterogeneous reaction of *B* occurring at the interface, one will reach:

$$|N_{BZ} - C_B v_{IZ}|_{z=0^-} = |N_{BZ} - C_B v_{IZ}|_{z=0^+} \quad \text{where } v_z = -\frac{dh}{dt}. \tag{3.4}$$

On the liquid side, the mass balance of liquid electrolyte will yield:

$$N_{BZ}(t) = C_l \frac{dh}{dt}, \tag{3.5}$$

where C_l is the molar concentration of *B* in liquid. Combining equation (3.5) and equation (3.3), one will reach:

$$\frac{d(h^2)}{dt} = \frac{2C_g D_{AB}}{C_l} ln\left(\frac{1-x_h}{1-x_0}\right). \tag{3.6}$$

By measuring *h* with time, one will be able to evaluate the binary diffusivity using equation (3.6). x_h can be assumed to be zero when mass transport outside of the tube is sufficiently fast and the outside air has an extremely low content of *B*. x_0 can be calculated using the vapor pressure of the solvent liquid. To calculate the diffusion coefficient (D_{AB}), a linear regression between h^2 and *t* is used.

For uncertainty analysis, equation (3.6) is rearranged as below,

$$D_{AB} = \frac{C_l}{2C_g ln\left(\frac{1}{1-x_0}\right)} \frac{\Delta h^2}{\Delta t}. \tag{3.7}$$

In the above, *h* and *t* are directly measured in the experiment. Then, the root mean square (RMS) is expressed as,

$$\sqrt{\overline{(\delta D_{AB})^2}} = \frac{C_l}{2C_g ln\left(\frac{1}{1-x_0}\right)} \sqrt{\frac{4h^2}{t^2}\overline{(\delta h)^2} + \frac{h^4}{t^4}\overline{(\delta t)^2}}\,. \tag{3.8}$$

The resolutions in the height and running time measurements are 0.5 mm and 2 min, respectively.

To validate the experimental design, water and ethanol were first employed as the testing liquid since their properties are well determined in the literature. In addition, three commonly used theoretical and empirical correlations are used for comparison: (1) Fuller, Schettler and Giddings (FSG), (2) Chapman and Enskog (CE), and (3) Slattery and Bird (SB). The properties of all the liquids and the correlations are summarized in Table 3.1 and Table 3.2, respectively.

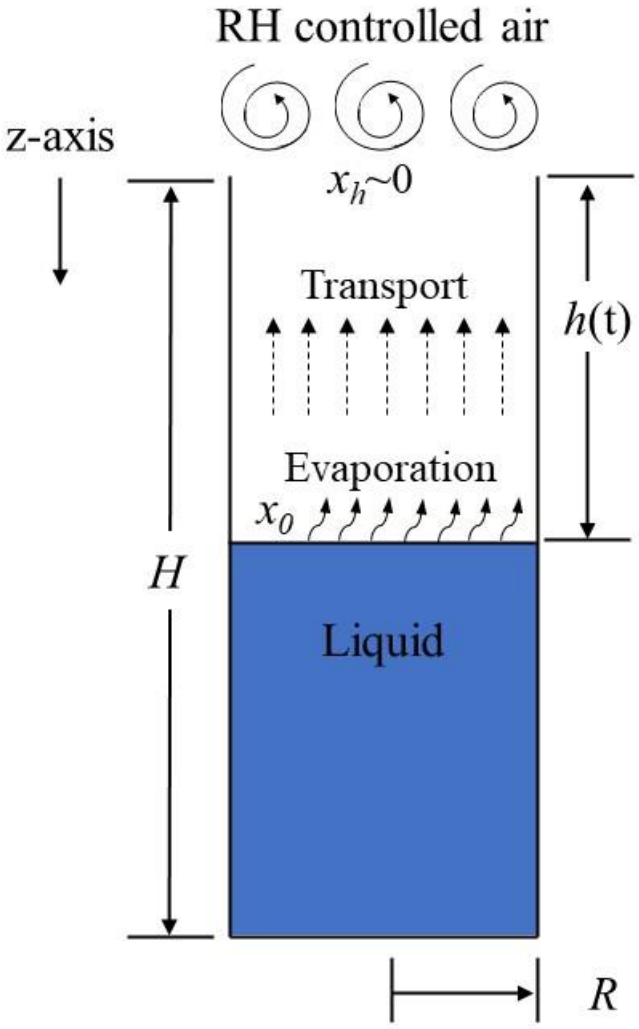

Figure 3.3 Schematic diagram of evaporation and transport in a vertical glass tube containing liquid exposed to ambient air.

Table 3.1 Properties of the electrolytes (DME, DMC, DEC, and PC), water, ethanol, and air for theoretical estimation of diffusivity.

	DME	DMC	DEC	PC	Water	Ethanol	Air
M (g/mol)	90.12	90.08	118.13	102.09	18.02	46.07	28.97
C_g (mol/m^3)	41.3	41.3	41.6	41.6	41.6	41.4	
ρ_{liq} (g m/L, 25°C)	0.867	1.069	0.975	1.204	0.997	0.789	
C_l (mol/m^3)	9.63×10^3	1.19×10^4	8.25×10^3	1.18×10^4	5.53×10^4	1.71×10^4	
P_{vap} (mmHg, 20°C)	48	18	10	0.13	17.5	44	
x_0 (20°C)	6.32×10^{-2}	2.37×10^{-2}	1.32×10^{-2}	1.71×10^{-4}	2.31×10^{-2}	5.79×10^{-2}	
$\sum V$	96.76	77.82	118.74	94.32	12.70	50.36	20.10
σ (Å)					2.641	4.530	3.711
ε/k_B(K)					809.1	362.6	78.6
k_BT/ε					1.083	1.617	
Ω					1.388	1.162	
T_c (K)					647.3	516.3	132.4
P_c (atm)					217.5	63.1	37.0
References	[50, 64]	[52, 64]	[51, 64]	[53, 64]	[64]	[64]	[64]

Table 3.2 Theoretical and empirical correlations for diffusion coefficients.

Model	Equation	Reference
Fuller, Schettler and Giddings (FSG)	$D_{AB} = 10^{-3} \frac{T^{1.75}\left(\frac{1}{M_A}+\frac{1}{M_B}\right)^{1/2}}{p[(\sum V_A)^{1/3}+(\sum V_B)^{1/3}]^2}$	[64]
Chapman and Enskog (CE)	$D_{AB} = \frac{1.86 \cdot 10^{-3} T^{1.5}\left(\frac{1}{M_A}+\frac{1}{M_B}\right)^{1/2}}{p\Omega\sigma_{AB}^2}$	[64]
Slattery and Bird (SB)	$D_{AB} = \frac{3.64\times10^{-4}}{P}\left(\frac{T}{\sqrt{T_{c,A}T_{c,B}}}\right)^{2.334}\left(P_{c,A}P_{c,B}\right)^{1/3}\left(T_{c,A}T_{c,B}\right)^{5/12}\sqrt{\frac{1}{M_A}+\frac{1}{M_B}}$	[65]

3.2.2 Experimental Setup

Following the theory and analysis, an experiment set for measuring the liquid height in the tube was designed with its schematic diagram shown in Figure 3.4. The tube with an inner diameter of 1 mm and length of 100 mm, filled with one type of liquid electrolyte, is placed in a chamber where ambient air under controlled conditions is circulated during the experiment. The liquid height is measured using a camera with a light source. In the experiment, all the electrolytes, water, and ethanol in each tube in the chamber were simultaneously tested. Relative humidity (RH) (nearly 0% and 50±5%) is controlled by dry air supplied to the chamber. The chamber temperature and pressure were maintained under 21±1°C and ambient pressure (1 atm). All experiments were triplicated to ensure reproductivity.

The advantage of this measurement is (1) that evaporation and diffusion are measured at the same time, (2) that it does not require many parameters unlike other models, (3) it does not need any expensive device to set up, but the results are compatible. In addition, unlike other

models, that are mostly empirical, the theoretical model is developed from continuum-based physics.

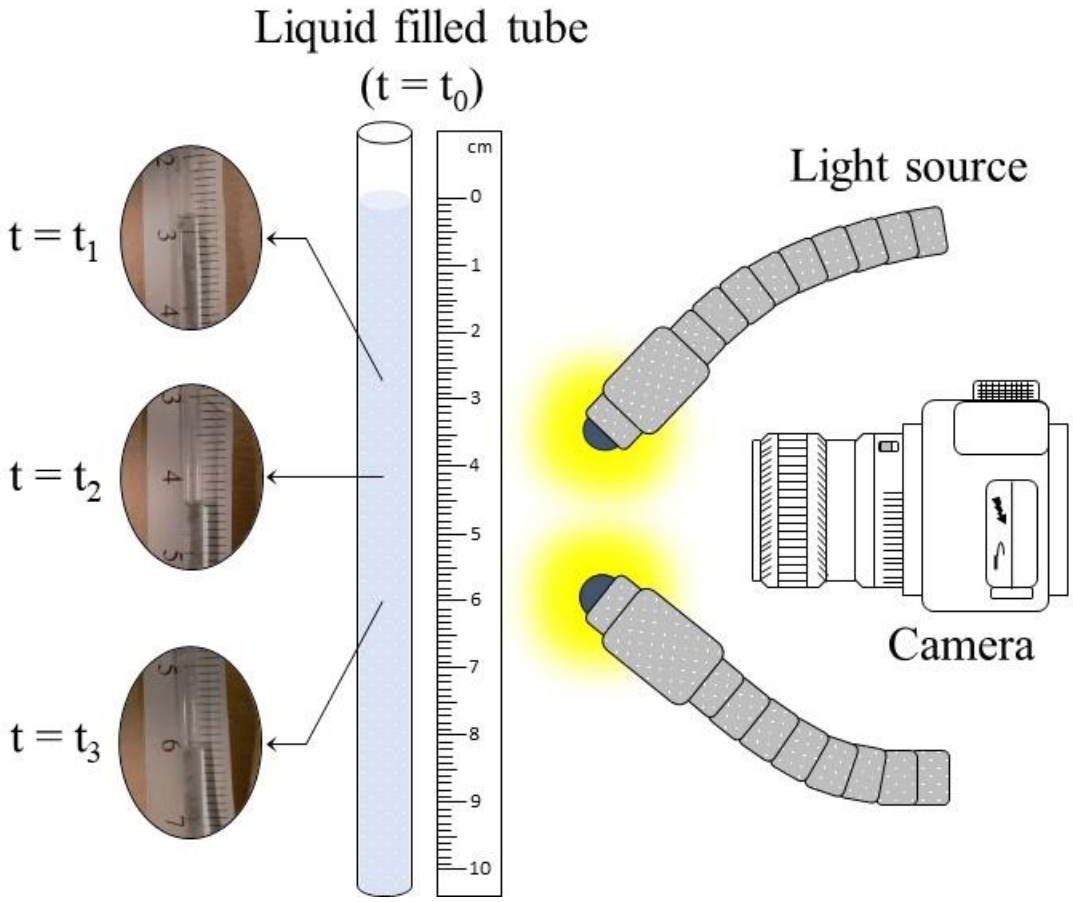

Figure 3.4 Schematic diagram of the experimental setup.

3.3 Results and Discussion

In order to measure diffusivity, the measurement of liquid heights of various electrolytes, water, and ethanol was taken continuously for 5-50 days depending on their evaporation rates. All the liquid samples except PC decreased their heights by evaporation with respect to the running time. Figure 3.5a shows the decrease in liquid heights in the tubes after exposure to ambient air. DME

has the fastest evaporation rate than the others in that ~4.6 cm of its height shrunk in 10 days. DMC and ethanol have comparable evaporation rates with a decrease in the height ~3.6 cm in 10 days. DEC and water evaporated in a similar trend with ~1.1 cm loss in 10 days. A negligible change was observed in the PC liquid height over 10 days, which is due to its extremely low evaporation rate. PC has only 0.13 mmHg of vapor pressure, thus it would not provide a measurable amount of evaporation during the experiment. Since no detectable height change of PC could be measured during the experimental timeframe, the formula cannot be applied directly to calculate its diffusivity. However, using the uncertainty in the height measurement (0.5 mm) and running time (10 days), we can estimate that the diffusivity of PC is less than 8.0×10^{-4} cm^2/s. The estimated diffusivity is much lower than that of 0.0826 cm^2/s from the FSG model. Based on the large difference between the two models, it may be attributed to the model's limitation that under the experimental conditions that limit evaporation, our model is not able to measure the diffusivity and the estimated value would be invalid. To overcome this issue, conducting the experiment at higher temperatures where PC evaporates with a measurable amount of volume is suggested. As to the impacts of RHs, an insignificant difference was observed between the RH=0% and 50% conditions. Figure 3.5b shows the evolutions of h^2 for all the cases, which are directly used to calculate the diffusion coefficients through linear regression using equation (3.6). The R^2 values for all the plots are larger than 0.998, meaning that the results are consistent without major deviations.

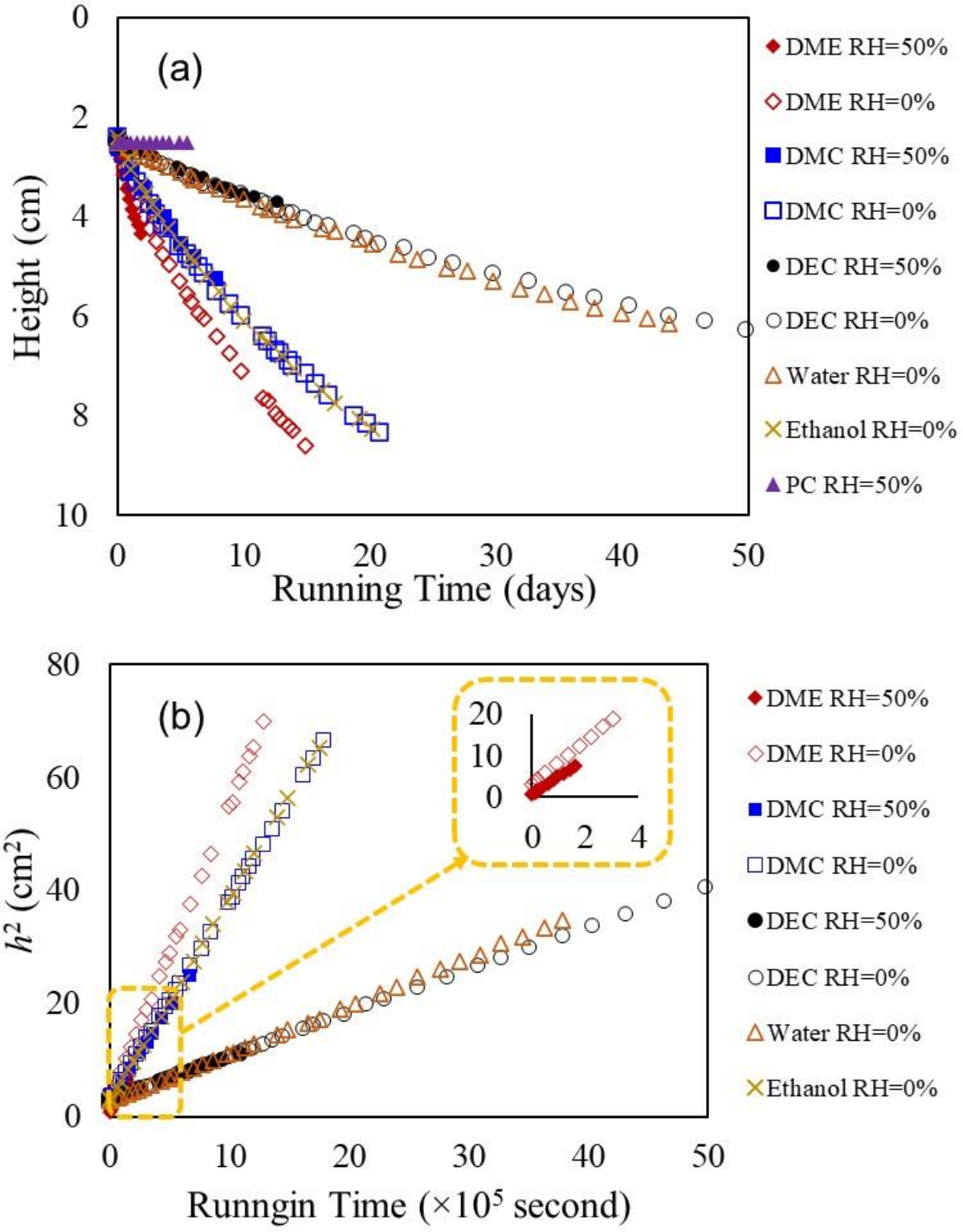

Figure 3.5 (a) Evaporation rates (b) and h^2 vs time plots of water, ethanol, DME, DEC, DMC, and PC.

The diffusion coefficient can be obtained by any point in the *h* curve in Figure 3.5. To evaluate the timescale for effective measurement using the model, the changes of measured diffusivity against the running time are shown in Figure 3.6. The diffusivities of DEC and ethanol are almost constant from the beginning to the end. However, those of DMC and water change by ~3% and ~17%, respectively, in the first 10-16 days. As to DME, the erratic diffusivity measured on day 6 is likely an outlier but the rest values are consistent. Based on our measurements, each run needs about 2-10 days to obtain a confident diffusion coefficient, depending on the liquid material. It should be noted that the effective running time for the measurement mainly depends on the measurement precision (uncertainty limitation). For the reliable diffusivity measurement, it was necessary to have distinguishable change in the liquid height. The effective running time can be significantly reduced with a better sensor that can precisely measure the liquid mass flux. Concerning the uncertainty, the calculation results of uncertainty analysis showed that the RMS values for all the samples were extremely small with the largest about 1.37×10^{-4} cm^2/s for water at RH=0%, only 0.062% deviation. The largest percentage uncertainty is 0.145% for DME at RH=50%, which is much smaller than the fluctuation magnitude in the calculated diffusivities changing with time.

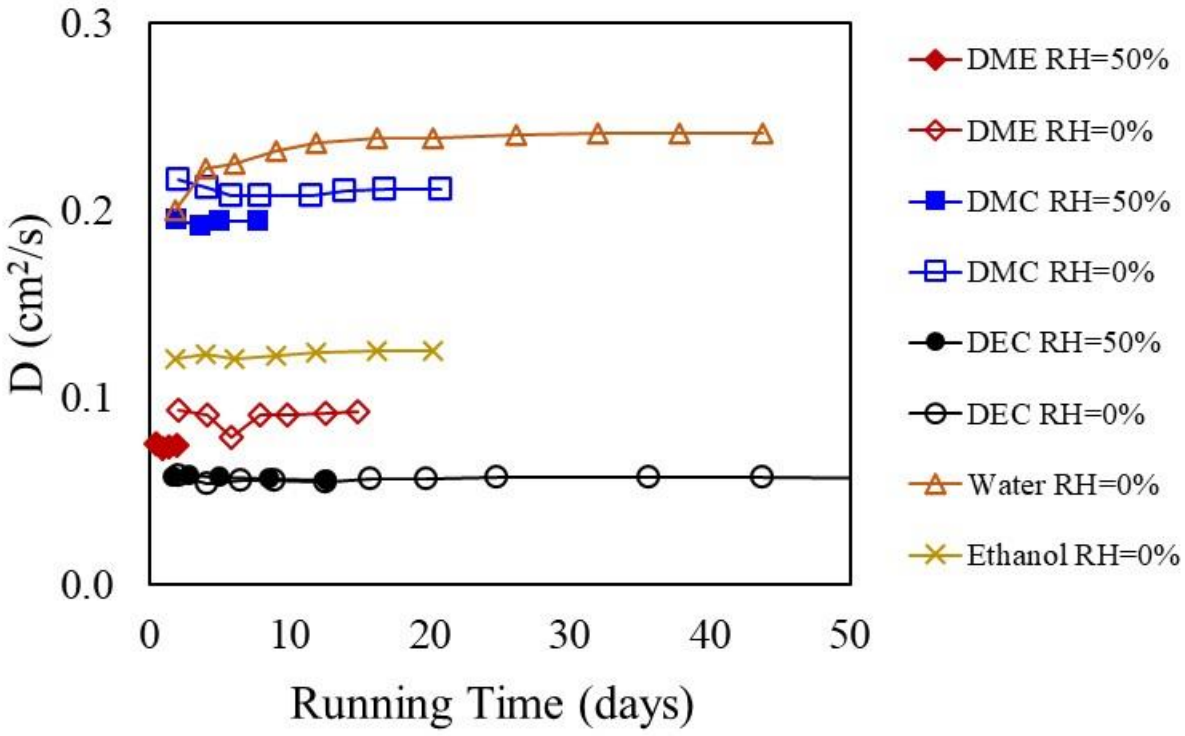

Figure 3.6 Changes of the measured diffusivities against the running time.

In order to validate the model and experimental method, the evaporation rates of water and ethanol were measured, and their diffusivity values were calculated using the experimental data. Then, they were compared with those calculated by other models (FSG, CE, and SB) in Table 3.2 and from the literature (Montgomery, Lee and Wilke, Chen and Othmer, and Lugg) [64-69]. Figure 3.7 shows that the measured diffusion coefficient of water in the present study is consistent with those estimated by other models and the references, and the diffusivity of the CE correlation has about 18% deviation from our experimental result. This can be explained by the fact that water is partially polarized by polar covalent bonding, while the CE model is primarily for non-polar gases. The result of ethanol is also consistent with other models and reference values as seen in Figure 3.7. It should be noted that even though ethanol is a polar molecule, the value estimated by the CE equation is close to the experimental result and other data. The largest deviation occurred for the

SB equation which predicts a 29% larger value than the experimental measurement. This deviation may be caused by the assumption of the SB model that there is an interdiffusion of water and a nonpolar gas. Based on the experimental results and theoretical estimations of the two popular solvents, the experimental design of the present study was validated.

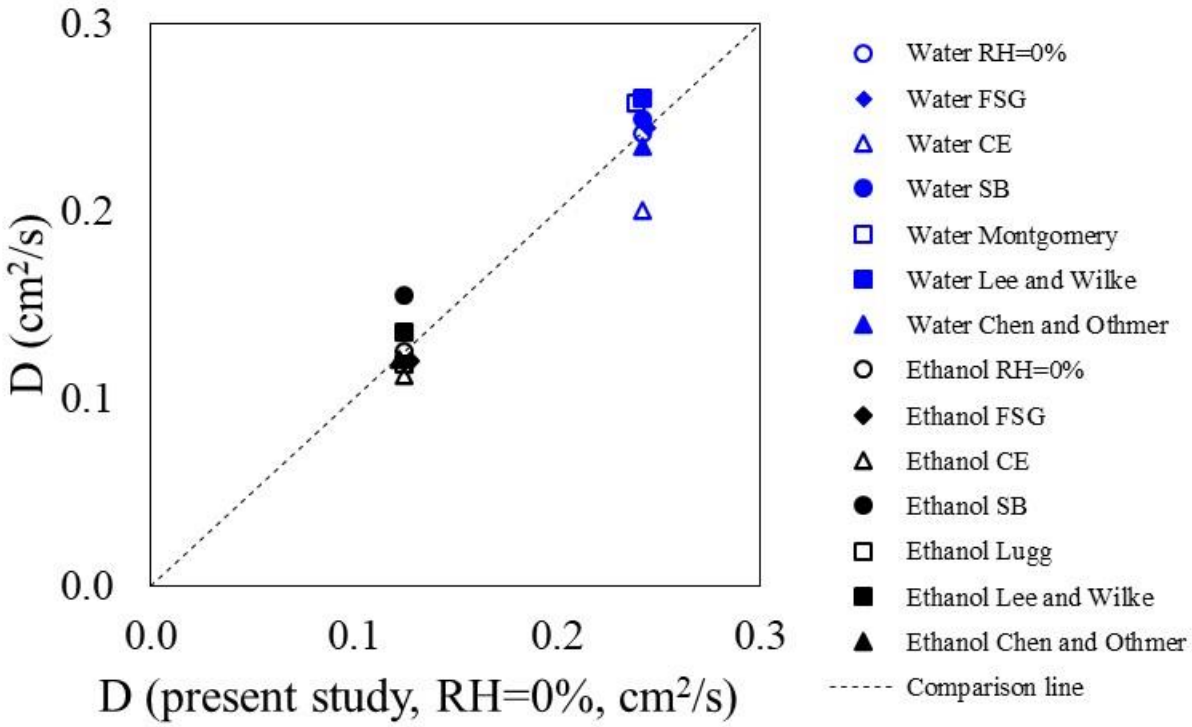

Figure 3.7 Comparison of the theoretical estimations and literature values with the present experimental measurement for water and ethanol [66-69].

Since PC did not show any considerable evaporation over 10 days, it failed to evaluate its diffusivity using the experimental design in the testing timeframe. The estimated value based on the uncertainty in the height measurement, which is $<8.0\times10^{-4}$ cm^2/s, is not listed in the following figures. Figure 3.8 compares the experimental results with the estimated diffusivities using the

FSG equation. The CE and SB equations were not used due to a lack of values for the model parameters. Since there is no tabulated value of the molar volume in the FSG equation for DME, DMC, and DEC, their molar volumes were estimated by using each atomic molar volumes (C, H, and O have 16.5 cm^3/g mol, 1.98 cm^3/g mol, and 5.48 cm^3/g mol, respectively). It should be noted that this estimate is a rough estimate. The diffusivity values of DME for both RH=0% and RH=50% cases are closed to the FSG estimation. The DEC values for both cases are slightly lower than the FSG estimation. The DMC's are, however, 113% and 133% larger under RH=50% and RH=0%, respectively, than the FSG estimation. This may be attributed to the rough evaluation of the molar volume of the organic solvents. The experimental results also show a slight difference in the diffusion coefficients between the two RH conditions. The diffusivities of DME, DMC, and DEC decrease by 20%, 8.5%, and 1.8%, respectively, when RH changes from 0% to 50%. Considering that DME is miscible with water (1000 g/L at 25°C [70]) while DMC is solube in water (139 g/L at 25°C [71]) and DEC is insoluble in water [51], it may be concluded that liquid with larger water solubility has more substantial decrease in the diffusivity measurement under higher RH. This may also be due to the fact that ambient water vapor dissolving in the organic solvents reduces the height loss during testing. This is also consistent with the results from Astrath et al. [72] that water vapor has a limited impact on changes in diffusivity for insoluble gases. Their findings showed only 17% increase in the diffusion coefficient of the ternary (O_2-N_2-H_2O) system when RH increased from 0% to 80% at 79 °C.

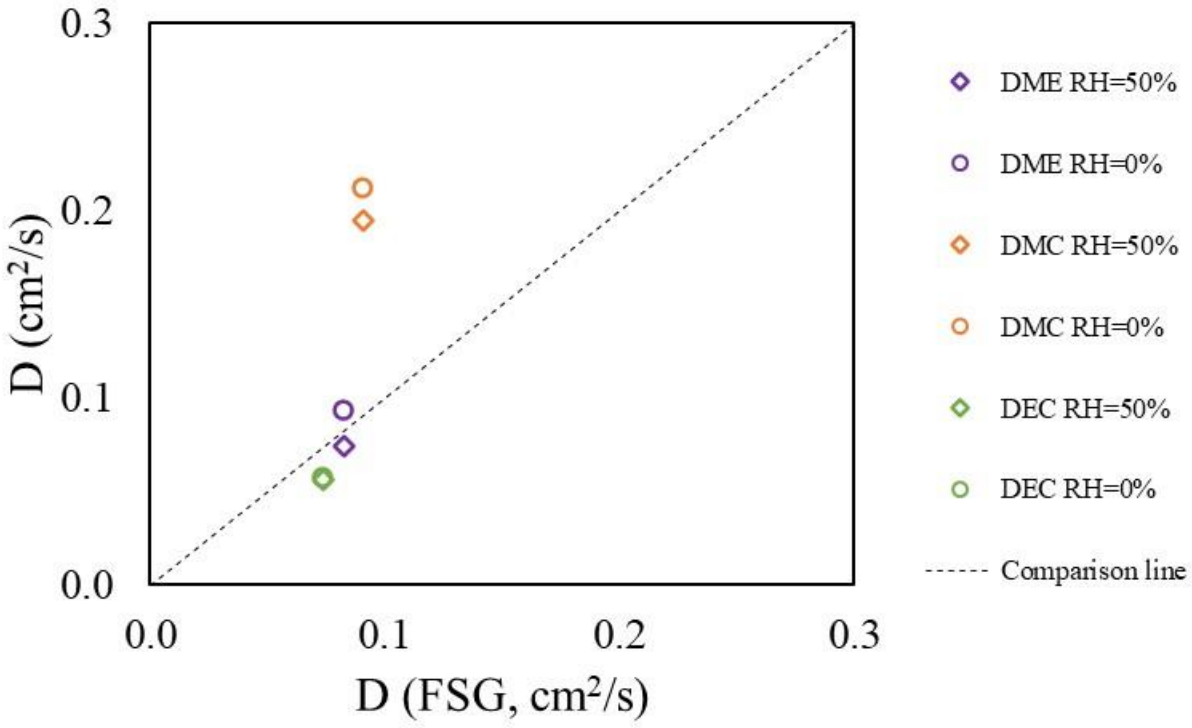

Figure 3.8 Comparisons of the diffusion coefficients measured in the present study with the predictions by the FSG model for DME, DMC, and DEC.

Stefan's solution to the evaporation-transport (diffusion) problem considers both evaporation-driven convection and diffusion (C&D) as described in equation (3.1). However, when considering diffusive transport only (D-O), the equation can be modified as shown below:

$$N_{BZ} = -C_g D_{AB} \frac{dx_B}{dz}. \tag{3.9}$$

Correspondingly, the solution of equation (3.9) can be found below:

$$\frac{d(h^2)}{dt} = -\frac{2C_g D_{AB} x_0}{C_l}, \tag{3.10}$$

To compare the diffusion coefficients between the C&D and D-O cases, the ratio between the C&D and D-O cases can be described below:

$$\frac{D_{\text{Diffusion Only}}}{D_{\text{Convection \& Diffusion}}} = -\frac{ln(1-x_0)}{x_0}. \tag{3.11}$$

Figure 3.9 shows the diffusivities estimated by considering the case of D-O (equation (3.10)) and the case of C&D (equation (3.6)) for water, ethanol, DME, DMC, and DEC. While DEC has the smallest difference of 0.7% due to the smallest x_0 of 1.32×10^{-2}, DME has the largest difference of 3.3% due to the largest x_0 of 6.32×10^{-2}. Ethanol, water, DMC have 3.0%, 1.2%, and 1.2% differences, respectively. As x_0 is the only variable in equation (3.11), the ratios of diffusion coefficients for the two cases vary with vapor pressure of liquid. RH does not impact the difference as it is not shown as a parameter in equation (3.11). A high molar fraction x_0 implies that the liquid is volatile.

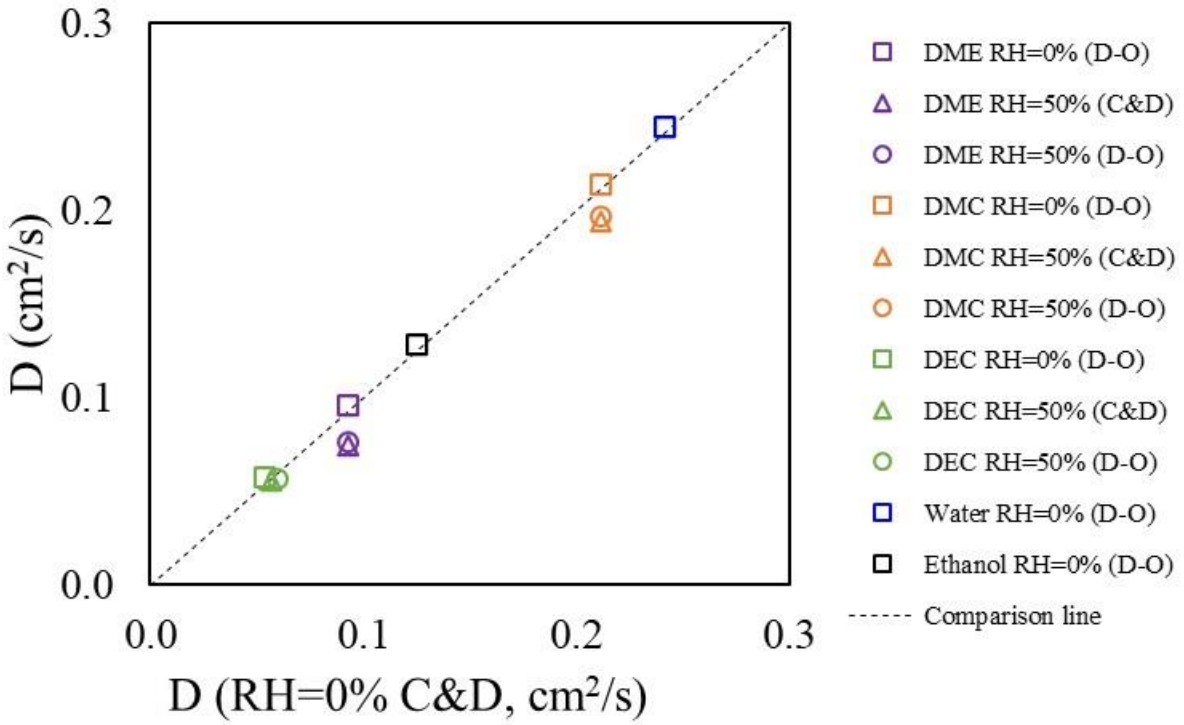

Figure 3.9 Comparisons of the diffusion coefficients calculated by the diffusion only (D-O) model (equation (3.10)) and the evaporation-driven convection and diffusion (C&D) model (equation (3.6)) using the experimental data.

3.4 Summary

This chapter proposed and discussed the experimental method to measure the diffusion coefficients and evaporation rates of organic solvents (DME, DMC, DEC, and PC) which are commonly used as nonaqueous electrolytes for light-metal batteries, such as Li-ion, Li-O_2, and Na-O_2 batteries. A 1-D evaporation-driven transport model was derived to build the relationship between the diffusion coefficients of organic solvents in ambient air and the height change of liquid in a tube. An evaporation experiment was designed to record the heights of various liquids with respect to the running time in a RH-controlled chamber. The experimental method was validated by comparing

the experimental results of two popular solvents, water and ethanol, of which parameters are well-known, with those estimated by other models and the literature data. The experimental results and calculated values in the present study are summarized in Table 3.3. The results were compared with several correlations and the literature data, showing good agreement. The diffusivity of PC was estimated with the uncertainty limits since it did not show any measurable change in the liquid height. The large difference of PC diffusivity between our model and the FSG model needs further investigation, such as repeating the experiment at a higher temperature. In addition, it was found that organic solvents with higher solubility in water had a larger decrease in the measured diffusivity when RH changes from 0% to 50%. This may be because, based on Raoult's law, water dissolving to the organic solvents with the higher solubility may slow down the molecular movement by changing the vapor pressure of solvents. The impact of evaporation-driven convectional transport on the diffusion coefficient measurement was also investigated using a model considering both evaporation-driven convection and diffusion and another model considering diffusion only. It was revealed that there is little difference between the diffusion coefficients calculated by the two models using the experimental data, thus the simpler model (diffusion only) suffices for the studied liquids. However, it should be noted that this simplification is valid only if the vapor pressure of a liquid is significantly smaller than the atmospheric pressure. The comparisons of changes in the diffusivity measurement against the running time show that the timescale for the diffusivity measurement is approximately 2-10 days for the studied liquids. The findings in this paper may be applied to investigate the lifetime of residual solvents, indoor solvent vapor transport, environmental contamination, and human health effect of harmful nonaqueous electrolytes that are widely used in light-metal batteries.

Table 3.3 Diffusion coefficients measured and calculated in the present study.

Diffusivity (cm^2/s)	DME	DMC	DEC	PC	Water	Ethanol
RH=0% (C&D)	0.0925	0.2116	0.0569	$<8.0\times10^{-4*}$	0.2415	0.1250
RH=0% (D-O)	0.0956	0.2141	0.0573		0.2444	0.1287
RH=50% (C&D)	0.0742	0.1943	0.0559			
RH=50% (D-O)	0.0766	0.1967	0.0562		0.2439	0.1197
FSG	0.0829	0.0908	0.0738	0.0826	0.2439	0.1197
CE					0.1999	0.1121
SB					0.2491	0.1544

*Estimation from uncertainty analysis

CHAPTER 4: Evaluation of Evaporation and Diffusion of Gas in Porous Media

Abstract

In this Chapter, a 1-D model of mass transfer with a porous layer was proposed and experiments to measure evaporation rates of liquids were conducted to validate the model. Diffusion resistance method was utilized to express the complex mass transfer including both diffusion in air and diffusion in porous media. From the diffusivity change against running time, it takes up to 10 days to acquire a stable diffusivity value, which is in a good agreement with the finding in Chapter 3. The estimated diffusivities of ethanol for the cases of perforated polymer plates bonded on the top of the liquid filled cylinders were in good agreement with experimental results. For the carbon paper cases, adding porous layers (carbon papers) showed effective reduction of solvent evaporation and the evaporation rates showed a reasonable trend regarding different porous conditions. However, the estimated correction constants were 1000 times smaller than the experimental results. To address the issue, three hypotheses are suggested, and the most possible hypothesis is that solubility between the liquid and porous material may have a critical impact on determining effective density.

4.1 Introduction

In the previous chapter, a diffusion model of evaporated organic solvent in ambient air has been theoretically developed and experimentally validated. In this chapter, evaporative and diffusive mass transfer of gaseous species through porous media is explored. Li-air battery uses porous structure carbon-based materials such as graphene nanosheets, carbon powder, hollow carbon fibers, and carbon papers as cathode electrodes [7, 38, 73]. In Li-air battery, oxygen is supplied to the electrolyte from the ambient air, therefore, maximizing the amount of oxygen into the cell improves the cell performance. On the other hand, minimizing electrolyte loss to the ambient air is also very important as loss of electrolyte reduces the battery performance and sometimes causes battery failure in severe cases. In addition to the battery performance, evaporated electrolyte solvents can be harmful for human health as described in the previous chapter. Therefore, the selection of the membrane for the cathode interface is one of the key factors in the development of Li-air battery.

There are many studies on diffusion in porous media reported for decades. Daneshpajooh et al. [74] investigated on the frictional models for membrane transport of gases. Their results were compatible with nonequilibrium thermodynamics. Webb [75] reported comparisons the Advective-Dispersive Model (ADM) and the Dusty-Gas Model (DGM) for combined advection and diffusion of gaseous species in porous media. In He-Ar case, DGM was better than ADM but in air-water system the differences between the two models were insignificant. The differences come from the ratio of molecular weights of the gaseous species; for the large cases, DGM is recommended. Tartakovsky and Dentz [76] reviewed two distinct approaches for diffusion models in porous media, starting from Brownian motion to Non-Fickian diffusion in porous media through Langevin model, Smoluchowski theory, and Knudsen diffusion. Pisani [77] conducted a

theoretical study on multi-component gas mixture diffusion through porous media. A 1-D solution was used, considering Stefan-Maxwell for the diffusion in multi-component gas mixtures, Knudsen for the diffusion inside a porous medium, and Darcy law for when the mean pore diameter is much larger than the molecular mean free path. The equations used in the literature have shown good agreement with experimental results, which validates the model reliability. However, in many practical cases with that many variables, variables cannot be controlled or are unknown. It is difficult to use these equations due to too many unknown parameters and the complexity of the equations. Due to such issues, a few simplified models have been used to approximately estimate effective diffusivity. In Bruggemann correction, the effective diffusivity in porous media can be expressed as [78]

$$D_{ij}^{\text{eff}} = \varepsilon^{1.5} D_{ij} \tag{4.41}$$

Note ε represents porosity, the ratio of pore volume to total volume. When tortuosity (τ) is considered, equation (4.1) can be modified as

$$D_{ij}^{\text{eff}} = \varepsilon^{\tau} D_{ij} \tag{4.42}$$

Tortuosity typically varies from 1.5 to 10, upon the pore structure.

In the high temperature conditions, another corrected equation is known more accurate [65]

$$D_{ij}^{\text{eff}} = \frac{\varepsilon}{\tau} D_{ij} \tag{4.43}$$

Those equations above have advantages due to their simple structure and small number of parameters. However, they raise doubts on validity when being given a new porous material since the equation structures are very simple and the tortuosity is not a parameter that is normally informed by the manufacturer nor easily measured. Thus, the present study began from validating

the equation with a simple porous structure and expanding to estimate and compare the effective diffusivity of water and ethanol vapor thorough two commercial carbon papers that are used for Li-air battery with the experimental results.

4.2 Method

4.2.1 Model Development

Figure 4.1 demonstrates a 1-D diffusion through porous media with evaporation-driven mass transport. Once the liquid is vaporized, the gaseous molecules move upward by convection and molecular diffusion. When the molecules reach the interface between air and porous media, they pass through the media with thickness (δ) by diffusion. However, due to the porous structure, the molecular diffusion will be impeded by blockage. The diffusivity in porous media will be lower than that in the air and needs to be corrected to effective diffusivity. Assuming the concentrations of vapor at the liquid-air interface and at the porous media-air interface and diffusivity in air (D_1) are given, the diffusion coefficient in the porous media (D_2) can be estimated. The idea for this model derivation comes from thermal resistance in Figure 4.2 and it is assumed to be eligible due to the analogy between heat transfer and mass transfer. Using this resistivity idea, Fick's law can be expressed as:

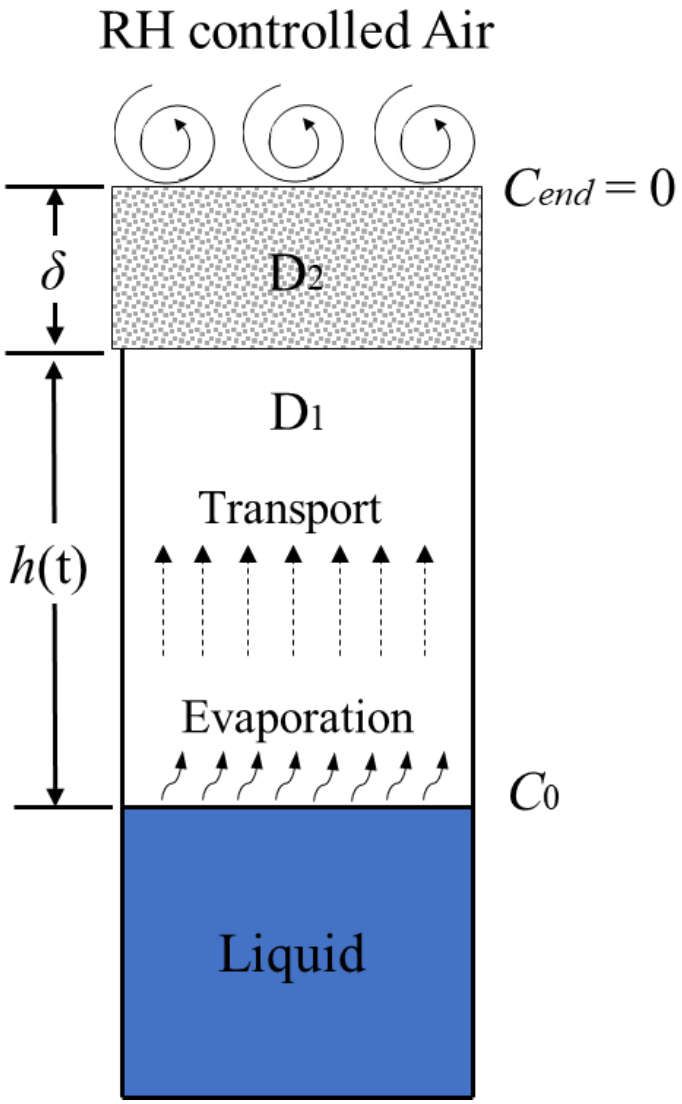

Figure 4.1 Schematic diagram of a 1-D evaporation-diffusion through porous media.

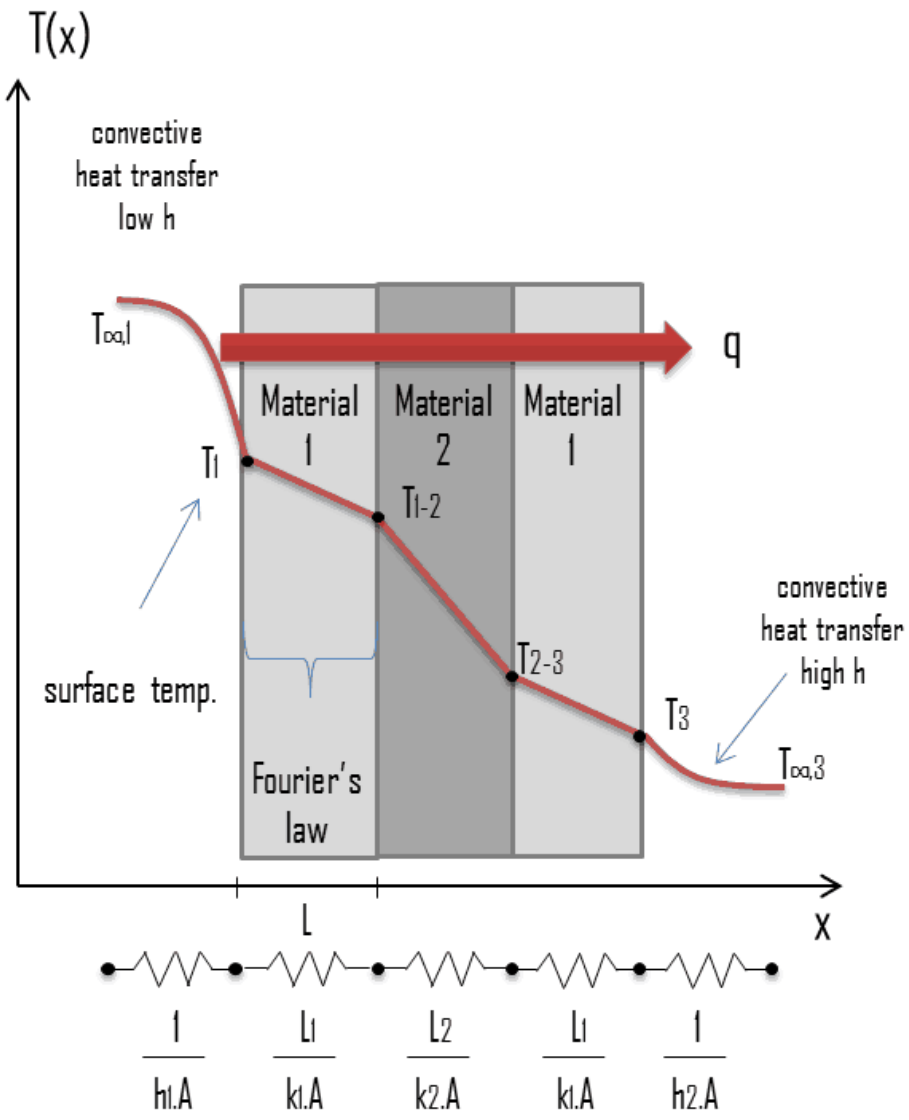

Figure 4.2 Example of thermal resistance [79].

$$j = \frac{1}{R_D}\Delta C \tag{4.44}$$

The mole flux (j) is equal to liquid concentration (C_L) times liquid height change over time ($dh(t)/dt$) and resistance R_D is the sum of the inverse of diffusivity divided by diffusional length. Equation (4.4) can be converted to

$$C_L \frac{dh(t)}{dt} = \frac{1}{\frac{h(t)}{D_1} + \frac{\delta}{D_2}} (C_0 - C_{end}) \tag{4.45}$$

where h(t) and δ indicate liquid height with respect to the time and thickness of the porous media, respectively. D_1 and D_2 are the diffusivities of vaporized solvent in air and porous media, respectively. The concentration at the porous media-air interface (C_{end}) is zero as the blowing dry air keeps the surface extremely low concentration of the vapor. Using the ideal gas law, the concentration of liquid-air interface (C_0) can be expressed as:

$$P_{vap} = C_0 RT \rightarrow C_0 = \frac{P_{vap}}{RT} \tag{4.46}$$

where P_{vap}, R, and T indicate vapor pressure of the liquid, universal gas constant, and temperature, respectively. Considering species conservation, $C_L = \rho_L / \mathrm{M}_i$, equation (4.5) is described as:

$$\frac{\rho_L}{M_i} \frac{dh(t)}{dt} = \frac{P_{vap}/RT}{\frac{h(t)}{D_1} + \frac{\delta}{D_2}} \tag{4.47}$$

where ρ_L and M_i represent liquid density and molecular weight of the liquid solvent, respectively. Equation (4.7) can be simplified as:

$$\frac{dh(t)}{dt} = \frac{D_1 D_2 M_i P_{vap}}{RT\rho_L (D_2 h(t) + D_1 \delta)} \tag{4.48}$$

Solving this 1st order ODE, the following equation can be found.

$$D_2 h(t) \frac{dh(t)}{dt} + D_1 \delta \frac{dh(t)}{dt} = \frac{D_1 D_2 M_i P_{vap}}{RT\rho_L} \tag{4.49}$$

To make it easier to integrate, equation (4.9) can be modified as:

$$\frac{D_2}{2}\frac{dh(t)^2}{dt} + D_1\delta\frac{dh(t)}{dt} = \frac{D_1 D_2 M_i P_{vap}}{RT\rho_L} \tag{4.50}$$

By integrating equation (4.10),

$$\frac{D_2}{2}\int_0^\tau \frac{dh(t)^2}{dt}dt + D_1\delta\int_0^\tau \frac{dh(t)}{dt}dt = \frac{D_1 D_2 M_i P_{vap}}{RT\rho_L}\int_0^\tau dt \tag{4.51}$$

$$\frac{D_2}{2}(h(t)^2 - h_0^2) + D_1\delta(h(t) - h_0) = \frac{D_1 D_2 M_i P_{vap}}{RT\rho_L}(t - t_0) \tag{4.52}$$

Finally, the effective diffusivity in the porous media can be expressed as:

$$D_2 = \frac{D_1\delta(h(t) - h_0)}{\frac{D_1 M_i P_{vap}(t - t_0)}{RT\rho_L} - \frac{1}{2}(h(t)^2 - h_0^2)} \tag{4.53}$$

It should be noted that D_2 depends on $h(t)^2$ as well as $h(t)$.

Once, the types of liquid solvent and porous media are determined, records of liquid height against the experiment running time are requested to measure the effective diffusivity.

4.2.2 Experimental Setup

Since the experiment is analogous to the experiment conducted in Chapter 3, the experimental setup was prepared similar to the diffusion measurement in Figure 3.4. However, in this experiment, a larger tube with 12 mm inner diameter and 120 mm length, filled with one type of liquid, was placed in the air-condition-controlled chamber to secure enough area for porous structures. The humidity and temperature of ambient air were controlled: The relative humidity (RH) was maintained as 0% by blowing dry air and the temperature was maintained 22±2°C under ambient pressure (1 atm).

Figure 4.3a shows the cylinder-porous media assembly, bonded by glue and Figure 4.3b shows the assemblies placed in the rack.

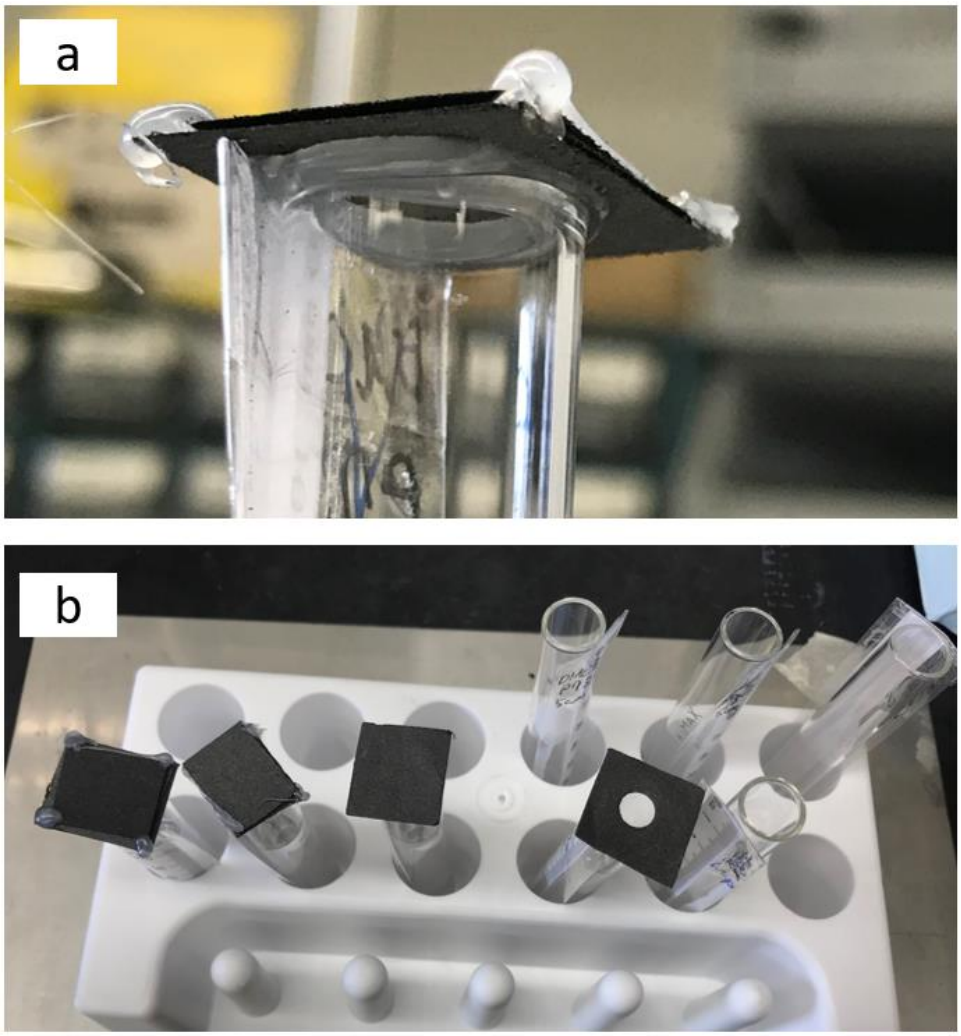

Figure 4.3 Cylinder-porous media assembly; (a) bonded by glue and (b) assemblies placed in the rack.

Diffusivities of the vapor in ambient air were measured to check if the modified experimental setup changes the results. Then, in order to validate the derived model, a single hole polymer with diameter of 5.27 mm and thickness of 6.15 mm was attached on the top of the cylinder. The single hole porous media can simplify the model as the tortuosity is 1 and porosity

is easily determined by the ratio of areas. The calculated porosity is 0.193. After validation with the single hole porous media, two commercial carbon papers (AvCarb P50, AvCarb P75) were employed to measure the effective diffusivities. AvCarb P50 (P50) and AvCarb P75 (P75) have nominal thickness of 0.184 mm and 0.205 mm, respectively. All experiments were repeated 3-4 times to ensure the reproductivity.

4.3 Results and Discussion

Since the cylinder dimensions are different from those used in Chapter 3, the diffusivities of water and ethanol in ambient air were measured by the same method used in Chapter 3. The results listed in Table 4.1 show that there are 18.2% and 14.4% increases in the diffusivity values for water and ethanol, respectively, which are reasonable deviation to be considered consistent.

Table 4.1 Comparison of diffusivity measured with small and large tubes.

	Water	Ethanol
Small cylinder (Ch. 3, cm^2/s)	0.242	0.125
Large cylinder (Ch. 4, cm^2/s)	0.286	0.143
Difference (%)	+18.2	+14.4

After validating the diffusion coefficients measured with the new experimental setup, single hole porous media bonded cylinders were prepared to validate the developed model. The porosity and tortuosity are already known so the effective diffusivity estimated by using equation

(4.2) was compared with the effective diffusivity estimated by the model (equation (4.13)). The effective diffusivity change with respect to the running time is plotted in Figure 4.4. The diffusivity of ethanol tends to be stabilized to 0.022 cm^2/s after 4 days from the beginning of evaporation while that of water vapor was stabilized to 0.056 cm^2/s after ~9 days running. As described in the Chapter 3.3, the effective running time is dependent on the measurement precision. Based on the equation (4.2), the porosity can be estimated to compare the model validity described as:

$$\frac{D_{ij}^{\text{eff}}}{D_{ij}} = \frac{D_2}{D_1} = \varepsilon^{\tau} \ (D_{ij}^{\text{eff}} = D_2, D_{ij} = D_1) \tag{4.54}$$

The comparison listed in Table 4.2 indicates that the two porosity values of water vapor are in good agreement and those of ethanol have 20% difference, but this is still under the consistent range.

Table 4.2 Comparison of estimated porosity using equation (4.13) with designed porosity determined by equation (4.14).

	Water	Ethanol
D (in air, cm^2/s)	0.286	0.143
D^{eff} (cm^2/s)	0.0564	0.0220
Estimated porosity (%)	19.8	15.4
Designed porosity (%)	19.3	

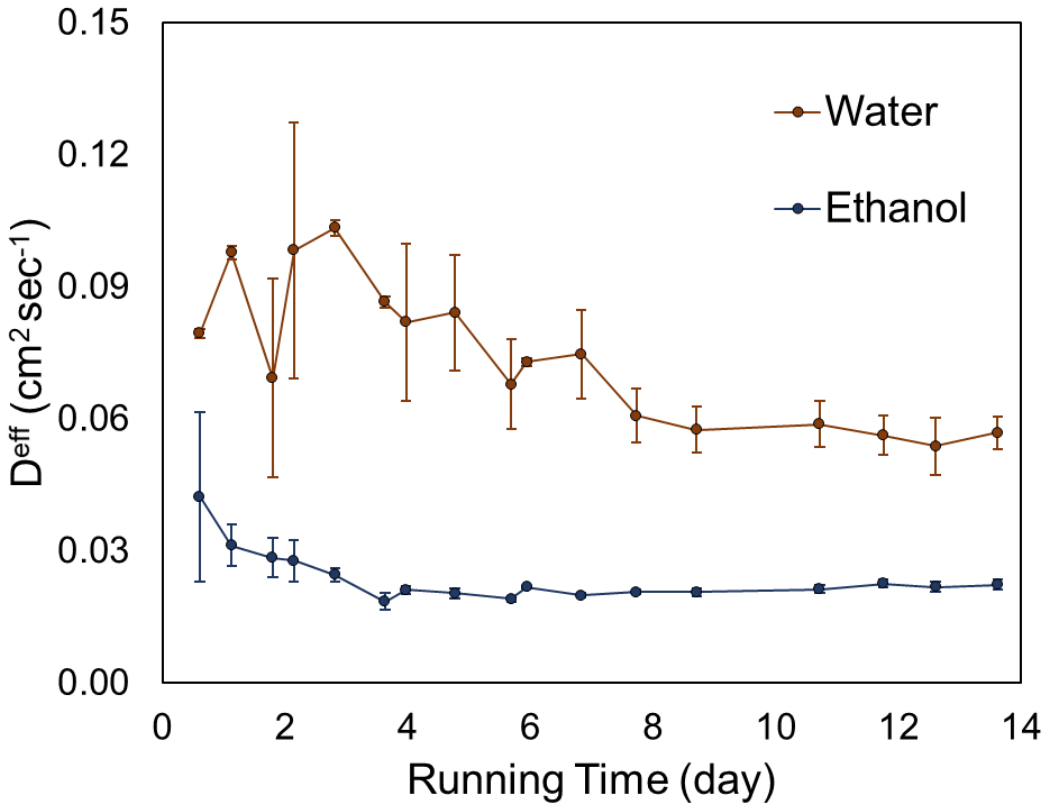

Figure 4.4 The effective diffusivity variance over the running time.

The next step was to validate the model with the practical porous media, commercial carbon papers. Figure 4.5 demonstrates the evaporation rate of ethanol under different porous conditions. An open cylinder was used as a reference and P50 carbon paper-cylinder assemblies of 4 configurations (a single layer with a single hole of 7.0 mm diameter, a single layer without any holes, 3 layers, and 5 layers) were used. Since there is no clear porosity and tortuosity data provided from the manufacturer, the correction constant (ε^{τ}) of the single layer with a hole is estimated to be a single layer of non-porous structure with the same size of the hole. Note the actual correction constant should be larger than the assumed value ($\varepsilon^{\tau}_{assumed} = 0.34$).

Evaporation rates of liquid ethanol under different porous conditions are shown in Figure 4.5. The open tube showed the fastest evaporation rate, then followed a single carbon paper with a hole, a single layer carbon paper, and 3-layer carbon paper in order. 5-layer carbon paper showed almost same result with that of the 3-layer. From the results, it was found that the evaporation depression effect is not linearly dependent on the number of carbon paper layers. For example, the evaporation rate of a single layer carbon paper decreased from 25 to 35% compared to the open tube case. Moreover, the evaporation rate of the 3-layer decreased from 29 to 40% compared to the open tube case. This may be explained by capillary action (wicking) in that liquid flows in narrow spaces (porous layer) due to the intermolecular forces between liquid and porous media. Even though it is not linearly dependent, it can be concluded that adding a porous layer effectively depresses the evaporation rate by limiting diffusion.

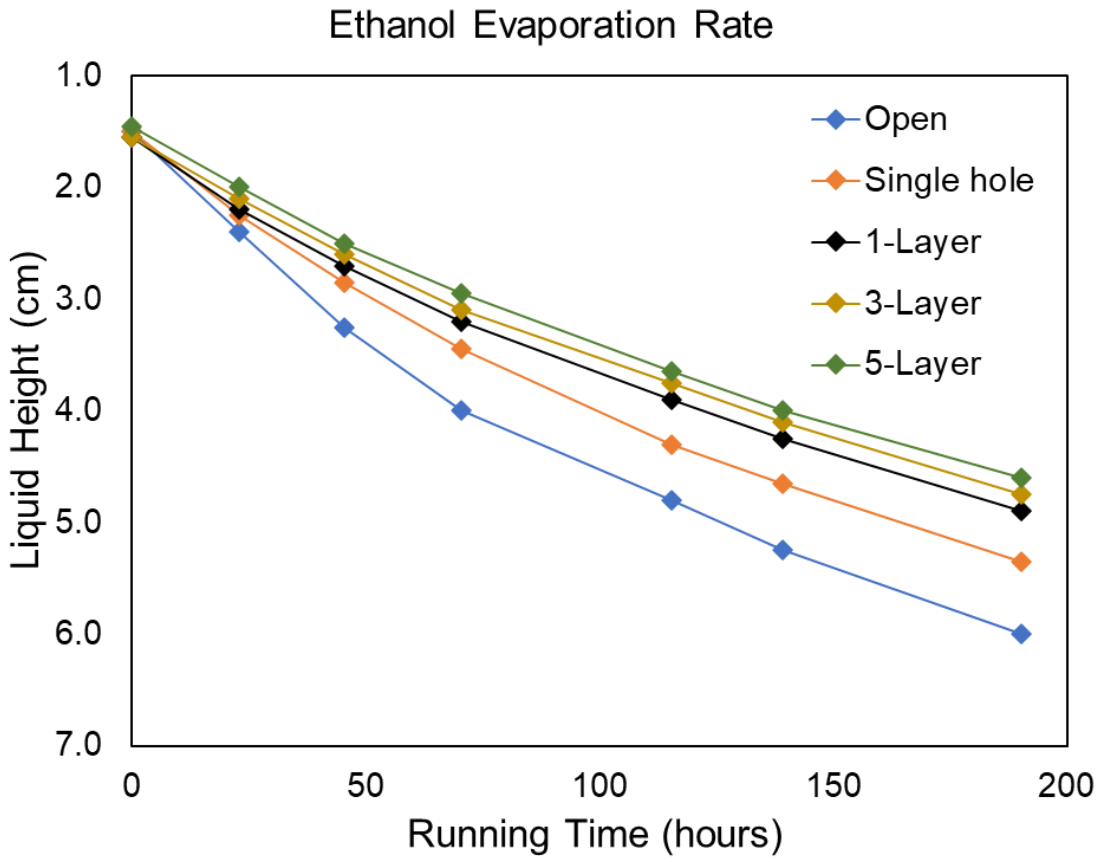

Figure 4.5 Evaporation rate of ethanol under different porous conditions.

The effective diffusivities calculated by using equation (4.13) are tabulated in Table 4.3. The average diffusivity of the open cylinder case is a bit larger than those measured in Chapter 3 (0.125 cm^2/s) and the current experimental setup validation (0.143 cm^2/s) but still in the reasonable range. However, the estimated correction constant for the single hole sample is almost 1000 times smaller than the assumed value. It should be noted that the correction constants for single layer, 3 layers, and 5 layers cases are closed together in values but becomes smaller as the number of the layers increase. This trend shows that the porous layers effectively depress the solvent evaporation and diffusion.

Table 4.3 The diffusivities estimated by using equation (4.13) for the open cylinder, a single layer with a single hole, a single layer without holes, 3 layers, and 5 layers of AvCarb P50 carbon paper.

Time (hrs)	Open (cm^2/s)	Single hole (cm^2/s)	1-Layer (cm^2/s)	3-Layer (cm^2/s)	5-Layer (cm^2/s)
23.0	0.15	7.20×10^{-05}	6.21×10^{-05}	5.22×10^{-05}	5.21×10^{-05}
45.5	0.18	6.56×10^{-05}	5.55×10^{-05}	5.04×10^{-05}	5.03×10^{-05}
70.5	0.19	6.13×10^{-05}	5.14×10^{-05}	4.81×10^{-05}	4.64×10^{-05}
115.5	0.17	5.38×10^{-05}	4.47×10^{-05}	4.17×10^{-05}	4.16×10^{-05}
139.1	0.18	5.02×10^{-05}	4.26×10^{-05}	4.01×10^{-05}	4.01×10^{-05}
190.2	0.17	4.49×10^{-05}	3.87×10^{-05}	3.69×10^{-05}	3.62×10^{-05}
Average *D*	**0.172**	$\mathbf{5.80\times10^{-05}}$	$\mathbf{4.92\times10^{-05}}$	$\mathbf{4.49\times10^{-05}}$	$\mathbf{4.45\times10^{-05}}$
Estimated ε^{τ}		$\mathbf{3.37\times10^{-04}}$	$\mathbf{2.86\times10^{-04}}$	$\mathbf{2.61\times10^{-04}}$	$\mathbf{2.59\times10^{-04}}$

Due to inconsistency between the diffusivities under the ethanol liquid and AvCarb P50 carbon paper condition estimated using equation (4.13) and equation (4.14), no further study has been conducted. Instead, some hypotheses on these large errors are suggested. The first hypothesis is that the derived equation has a problem in the assumptions or derivation. However, this hypothesis cannot explain the consistent results for the single hole polymer cases. The second hypothesis is that the derived model has limitations, such as that it is invalid for microporous structure due to Knudsen diffusion or that it is valid only with a certain range of thickness of porous

media. With the similar consideration, the precision of the current experimental setup is not enough to measure commercial carbon papers, considering the polymer's thick thickness of 6.15 mm while the carbon paper's thin thickness of ~0.2 mm. For example, as shown in Figure 4.3a, the sealing made from glue may not be able to perfectly prevent the gas leakage from passing though unexpected pathways. In addition, unclear thickness of the carbon paper may result in the error, e.g., P75 has two nominal thicknesses in different pressure conditions (0.245 mm at 1 psi and 0.205 mm at 7.3 psi). The last hypothesis is that the model has to consider solubility between the pore material and vaporized liquid. This may be a critical parameter because noticeable size of circular-shaped wet surfaces on the porous media have been frequently observed during the experiment. When vapor is condensed on the porous media, it may block the pathway of the vapor diffusion, which would significantly reduce the correction constant due to decreased active porous volume as well as absorbance of vapor to the condensed liquid surface. To understand condensation effect, the solubility of porous media and liquid solvent needs to be investigated and the effective active area of wet surface needs to be considered.

4.4 Summary

In this chapter, effective diffusivity in porous media has been estimated with a 1-D model derived using mass transfer resistor sub-model and the model was experimentally validated. A resistance consisting of molecular diffusion in air and diffusion in porous media is used for the 1-D steady-state mass transfer equation. The effective density can be estimated from the properties of vaporized liquid, thickness of the porous media, and the data of liquid height change against evaporation time. The model validity was examined by comparison with experimental data. A polymer plate with a single hole was employed to simplify the complexity as its tortuosity is a constant of 1 and porosity is easily measured. The experimental results with water and ethanol

have a good agreement with the estimated values. To prove the model validity in a practical use, each of two types of carbon papers was attached on the top of the cylinders filled with the liquids. The results were inconsistent with the experimental results in that they have 1000 times difference in the estimated correction constants. Evaporation rates of the carbon paper experiments indicate that the evaporation trend makes sense because the samples with straighter pathways for the vapor (less volume of porous media and with a single hole) showed larger evaporation rate. To address the larger errors between experimental results and the model estimations, three hypotheses are suggested. The first one is the model's inherent invalidity. However, this may not explain the good agreement in the results for the perforated polymer cases. The second hypothesis is unrecognized limitations in the model or experimental setup. It is possible that the model is not valid for microporous structure or porous media with a very thin thickness. The imprecise experimental setup may be able to explain the large error for the carbon paper experiments. The third hypothesis is about solubility between the porous media and liquid. When vaporized liquid is condensed in the porous media, the effective porous volume decreases as a result, and this can possibly largely decrease the measured effective diffusivity. It is recommended to investigate the solubility effect and to measure effective porous area during the experimental runs in order to improve the model validity. Also, the effective running time of diffusivity measurement was studied and the results indicate that it takes up to 10 days to be stable in diffusivity, which is consistent with the previous results in Chapter 3.

CHAPTER 5: Conclusion and Future Work

The dissertation explored the mass transfer of battery organic electrolyte with theoretical and experimental approaches. The study started from the consideration of increasing demand of the global energy conversion due to increasing global population and energy consumption per capita. Battery is currently the most popular and potential technology to effectively store and supply energy. Lithium based batteries, including Li-ion and Li-air, have drawn attention due to their light weight and lowest electronegativity of Li metal. However, Li-ion battery needs large improvements to fulfill the high specific energy needed for portable devices and electric vehicles and to make it secure in the events of physical impact and damage. Li-air battery needs far more improvements in that its commercialization has not yet been done due to its critical issues, such as voltage loss by discharge product precipitation and electrolyte consumption and loss to the ambient air. Such problems critically reduce the number of rechargeable battery cycles. Electrolyte plays a key role in determining Li-ion and Li-air battery performance and longevity. Therefore, the present study focused on three subjects: Spatial variation of cathode reaction rates in lithium-air batteries, Molecular diffusion and evaporation rate of battery organic electrolytes in ambient air, and evaluation of evaporation rate and diffusivity of gas in porous media.

In the first subject, a model of 1-D reaction and diffusion transport was employed. For the reaction, Tafel equation, an approximation form of the Butler-Volmer equation, is utilized to approximate the reaction rate. The simplified model with non-dimensionalization is characterized by *Damköhler* number (*Da*) and transfer coefficient (β). After a single layer model was developed, a model for multi-layer cathode was derived to optimize the cathode design for the purpose of minimizing the spatial variation of the reaction rates. From the case study, the effect of *Da*, β, and

baseline data on an optimal multi-layer cathode design was explored. In addition, the results provided practical data to evenly distribute the O_2 concentration reduction. The 3-D plot for the spatial variation of current density with respect to D_1 and D_2 may provide a good guideline in designing double-layer Li-air cathode. Based on the current research achievement, further studies can be suggested. One is to investigate impact of Li-Ox precipitates on battery discharge performance. Voltage loss by Li-Ox precipitations is a critical issue in Li-air battery, disrupting the battery commercialization. Experimental approach to measure the precipitation production and deposit is of importance to develop its prediction model. It is also recommended to use the models from literature and to compare the estimated values with the experimental data. Such studies are helpful in the battery development, and can ultimately facilitate commercialization of Li-air battery.

In the second subject, a 1-D evaporation-driven convection-diffusion model was proposed to estimate the diffusivity of organic solvents in ambient air. The organic solvents are 1,2-dimethoxyethane (DME), dimethyl carbonate (DMC), diethyl carbonate (DEC), and propylene carbonate (PC) which are typical electrolytes for light metal batteries. The model estimations were compared with the experimental results to prove its validity. The experiment was to measure evaporation rates of liquid solvents in narrow cylinders that are placed in an environment-controlled chamber. To validate the experiment setup, the data and other model predictions from literature for water and ethanol are compared with those measured from the present study. After proving that the results in this study were consistent with other literature data, diffusivities of organic solvents were found; DME (0.0925 cm^2/s), DMC (0.2116 cm^2/s), and DEC (0.0569 cm^2/s). The PC testing failed due to a liquid loss smaller than the measurement uncertainty resulting from its slow evaporation rate under the experimental condition. In addition, the diffusivity of organic

solvents with higher solubility in water tend to decrease more when RH changes from 0% to 50%. Raoult's law may explain this as water contents dissolved in the organic solvents may lower the vapor pressure of liquids. The results of this study will be useful in predicting diffusive behavior of exposed battery electrolyte to ambient air and determining public health guideline.

In addition to the diffusive mass transport in ambient air in the second subject, the third subject dealt with impact of a porous layer on the diffusive mass transport. Using a diffusion resistor sub-model, a 1-D model considering evaporation-driven convection-diffusion in air and diffusion in porous media was proposed to estimate effective diffusivity. The model validity was investigated by the comparison of the model estimation with the experimental results. For a single hole polymer plate as a porous media, the diffusivities are in good agreement. The diffusivity changes of water and ethanol against time indicated ~9 days of running time is required to obtain stable results, which is consistent with ~10 days effective running time found in the second subject. In the experiments with commercial carbon papers, the results were inconsistent with the estimations by the model, showing about 1,000 times difference in the correction constants. To address this issue, some hypotheses were suggested to account for the issue. One most possible hypothesis is to consider solubility between the porous media and liquid. Condensed liquid in the carbon papers may decrease the effective porous volume and accordingly, slow down the mass transfer through the paper. In order to address this, the suggested work is to investigate the solubility effect and to measure effective area of the porous media during the experiments. Another suggested future work is to simulate diffusive mass transfer of vaporized organic solvents under the room condition to predict time-dependent vapor concentration distributions. Electrolyte mass transfer outside does not bring out critical heal issues because it will rapidly spread by convection to a safe level However, in room condition, this could be dangerous. The results can be useful for

human health effect predictions in consideration of USA's Protective Action Criteria (PAC). PACs levels of organic solvents are listed in Table 5.1.

Table 5.1 Protective Action Criteria levels for battery electrolyte solvents [80].

	PAC-LEVEL1	**PAC-LEVEL2**	**PAC-LEVEL3**
Effect	Mild, transient health effects.	Irreversible or other serious health effects, impaired ability to take protective action.	Life-threatening health effects.
DME (mg/m^3)	2	22	280
DMC (mg/m^3)	39	430	2600
DEC (mg/m^3)	2	22	340
PC (mg/m^3)	3.3	37	220

Nomenclature

a	surface-to-volume ratio
C_i	molar concentration of species i
D_i	diffusion coefficient of species i
Da	*Damköhler* number
F	Faraday's constant
h	height of liquid
I	current density
j	mole flux
j_c	transfer current density
k	reaction coefficient
k_B	Boltzmann constant
M	molar mass
N	molar number
n	number of electrons
P	pressure in atmosphere
P_c	critical pressure
P_{vap}	vapor pressure
R	Universal gas constant
R_D	diffusion resistance
t	running time
T	temperature
T_c	critical temperature

u velocity in x-direction

U_0 equilibrium potential

v_{IZ} volume at the surface

$\sum V$ atomic diffusion volume

x_0 molar fraction at the interface

x_h molar fraction at the top of the glass tube

x_i molar fraction of species i

Greek

β transfer coefficient

δ thickness

ε porosity or energy of interaction (Chapter 3)

ε^{τ} correction constant

η surface overpotential

ρ density

σ collision diameter

τ tortuosity

Φ phase potential

Ω dimensionless quantity depending on an integration of the interaction between two species

Superscripts and Subscripts

e electron

eff	effective value
end	value at the end
g	gaseous component
l (*L*)	liquid component
0	value at the initial or bottom
ref	reference value

References

[1] D. Larcher, J.M. Tarascon, Towards greener and more sustainable batteries for electrical energy storage, Nat Chem, 7 (2015) 19-29.

[2] U.S.Energy Information Administration, What is U.S. electricity generation by energy source?, in, 2018.

[3] P.G. Bruce, S.A. Freunberger, L.J. Hardwick, J.M. Tarascon, Li-O-2 and Li-S batteries with high energy storage, Nat Mater, 11 (2012) 19-29.

[4] M. Mirzaeian, P.J. Hall, Preparation of controlled porosity carbon aerogels for energy storage in rechargeable lithium oxygen batteries, Electrochim Acta, 54 (2009) 7444-7451.

[5] Y. Gao, C. Wang, W.H. Pu, Z.X. Liu, C.S. Deng, P. Zhang, Z.Q. Mao, Preparation of high-capacity air electrode for lithium-air batteries, International Journal of Hydrogen Energy, 37 (2012) 12725-12730.

[6] C.O. Laoire, S. Mukerjee, K.M. Abraham, E.J. Plichta, M.A. Hendrickson, Elucidating the Mechanism of Oxygen Reduction for Lithium-Air Battery Applications, J Phys Chem C, 113 (2009) 20127-20134.

[7] Y.L. Li, J.J. Wang, X.F. Li, D.S. Geng, R.Y. Li, X.L. Sun, Superior energy capacity of graphene nanosheets for a nonaqueous lithium-oxygen battery, Chem Commun, 47 (2011) 9438-9440.

[8] Y.C. Lu, H.A. Gasteiger, M.C. Parent, V. Chiloyan, Y. Shao-Horn, The Influence of Catalysts on Discharge and Charge Voltages of Rechargeable Li-Oxygen Batteries, Electrochemical and Solid State Letters, 13 (2010) A69-A72.

[9] K.M. Abraham, Z. Jiang, A polymer electrolyte-based rechargeable lithium/oxygen battery, J Electrochem Soc, 143 (1996) 1-5.

[10] X.H. Yang, P. He, Y.Y. Xia, Preparation of mesocellular carbon foam and its application for lithium/oxygen battery, Electrochemistry Communications, 11 (2009) 1127-1130.

[11] Y. Wang, Modeling discharge deposit formation and its effect on lithium-air battery performance, Electrochim Acta, 75 (2012) 239-246.

[12] Y. Wang, Z. Wang, H. Yuan, T.Q. Li, Discharge Oxide Storage Capacity and Voltage Loss in Li-Air Battery, Electrochim Acta, 180 (2015) 382-393.

[13] Y. Wang, H. Yuan, Discharge Precipitate's Impact in Li-Air Battery: Comparison of Experiment and Model Predictions, J Electrochem Soc, 164 (2017) A2283-A2289.

[14] Y. Wang, S.C. Cho, Analysis of Air Cathode Perfomance for Lithium-Air Batteries, J Electrochem Soc, 160 (2013) A1847-A1855.

[15] X.Q. Zeng, G.L. Xu, Y. Li, X.Y. Luo, F. Maglia, C. Bauer, S.F. Lux, O. Paschos, S.J. Kim, P. Lamp, J. Lu, K. Amine, Z.H. Chen, Kinetic Study of Parasitic Reactions in Lithium-Ion Batteries: A Case Study on LiNi0.6Mn0.2Co0.2O2, Acs Appl Mater Inter, 8 (2016) 3446-3451.

[16] A.C. Luntz, B.D. McCloskey, Nonaqueous Li-Air Batteries: A Status Report, Chem Rev, 114 (2014) 11721-11750.

[17] Y. Yamada, M. Yaegashi, T. Abe, A. Yamada, A superconcentrated ether electrolyte for fast-charging Li-ion batteries, Chem Commun, 49 (2013) 11194-11196.

[18] K. Xu, Electrolytes and Interphases in Li-Ion Batteries and Beyond, Chem Rev, 114 (2014) 11503-11618.

[19] M. Gauthier, T.J. Carney, A. Grimaud, L. Giordano, N. Pour, H.H. Chang, D.P. Fenning, S.F. Lux, O. Paschos, C. Bauer, F. Magia, S. Lupart, P. Lamp, Y. Shao-Horn, Electrode-

Electrolyte Interface in Li-Ion Batteries: Current Understanding and New Insights, J Phys Chem Lett, 6 (2015) 4653-4672.

[20] H.H. Zheng, J. Li, X.Y. Song, G. Liu, V.S. Battaglia, A comprehensive understanding of electrode thickness effects on the electrochemical performances of Li-ion battery cathodes, Electrochim Acta, 71 (2012) 258-265.

[21] H. Yuan, J.A. Read, Y. Wang, Capacity loss of non-aqueous Li-Air battery due to insoluble product formation: Approximate solution and experimental validation, Mater Today Energy, 14 (2019).

[22] L.A. Tinker, Battery case leakage detector, US Patent No. US5399445A, in 1994.

[23] S. Jung, Secondary battery having safety vent, US Patent No. US8273473B2, in 2012.

[24] P. Masset, R.A. Guidotti, Thermal activated (thermal) battery technology - Part II. Molten salt electrolytes, J Power Sources, 164 (2007) 397-414.

[25] P. Albertus, G. Girishkumar, B. McCloskey, R.S. Sanchez-Carrera, B. Kozinsky, J. Christensen, A.C. Luntz, Identifying Capacity Limitations in the Li/Oxygen Battery Using Experiments and Modeling, J Electrochem Soc, 158 (2011) A343-A351.

[26] R.E. Williford, J.G. Zhang, Air electrode design for sustained high power operation of Li/air batteries, J Power Sources, 194 (2009) 1164-1170.

[27] V. Viswanathan, K.S. Thygesen, J.S. Hummelshoj, J.K. Norskov, G. Girishkumar, B.D. McCloskey, A.C. Luntz, Electrical conductivity in Li2O2 and its role in determining capacity limitations in non-aqueous Li-O-2 batteries, Journal of Chemical Physics, 135 (2011).

[28] X.L. Li, A. Faghri, Optimization of the Cathode Structure of Lithium-Air Batteries Based on a Two-Dimensional, Transient, Non-Isothermal Model, J Electrochem Soc, 159 (2012) A1747-A1754.

[29] P. Andrei, J.P. Zheng, M. Hendrickson, E.J. Plichta, Modeling of Li-Air Batteries with Dual Electrolyte, J Electrochem Soc, 159 (2012) A770-A780.

[30] U. Sahapatsombut, H. Cheng, K. Scott, Modelling the micro-macro homogeneous cycling behaviour of a lithium-air battery, J Power Sources, 227 (2013) 243-253.

[31] K. Yoo, S. Banerjee, P. Dutta, Modeling of volume change phenomena in a Li-air battery, J Power Sources, 258 (2014) 340-350.

[32] A.V. Sergeev, A.V. Chertovich, D.M. Itkis, E.A. Goodilin, A.R. Khokhlov, Effects of cathode and electrolyte properties on lithium-air battery performance: Computational study, J Power Sources, 279 (2015) 707-712.

[33] M. Mayur, W.G. Bessler, Two-Dimensional Computational Fluid Dynamics Analysis of Transport Limitations of Different Electrolyte Systems in a Lithium-Air Button Cell Cathode, J Electrochem Soc, 164 (2017) E3489-E3498.

[34] Y. Wang, Analysis of the key parameters in the cold start of polymer electrolyte fuel cells, J Electrochem Soc, 154 (2007) B1041-B1048.

[35] J. Read, K. Mutolo, M. Ervin, W. Behl, J. Wolfenstine, A. Driedger, D. Foster, Oxygen transport properties of organic electrolytes and performance of lithium/oxygen battery, J Electrochem Soc, 150 (2003) A1351-A1356.

[36] X.Z. Wu, T. Morikawa, K. Uchiyama, T. Hobo, Noncontact and noninvasive monitoring of gas diffusion from aqueous solution to aprotic solvent using the optical beam deflection method, J Phys Chem B, 101 (1997) 1520-1523.

[37] C.O. Laoire, S. Mukerjee, K.M. Abraham, E.J. Plichta, M.A. Hendrickson, Influence of Nonaqueous Solvents on the Electrochemistry of Oxygen in the Rechargeable Lithium-Air Battery, J Phys Chem C, 114 (2010) 9178-9186.

[38] Y.C. Lu, D.G. Kwabi, K.P.C. Yao, J.R. Harding, J.G. Zhou, L. Zuin, Y. Shao-Horn, The discharge rate capability of rechargeable Li-O-2 batteries, Energ Environ Sci, 4 (2011) 2999-3007.

[39] B. Dunn, H. Kamath, J.M. Tarascon, Electrical Energy Storage for the Grid: A Battery of Choices, Science, 334 (2011) 928-935.

[40] X. Shen, H. Liu, X.B. Cheng, C. Yan, J.Q. Huang, Beyond lithium ion batteries: Higher energy density battery systems based on lithium metal anodes, Energy Storage Mater, 12 (2018) 161-175.

[41] T. Placke, R. Kloepsch, S. Duhnen, M. Winter, Lithium ion, lithium metal, and alternative rechargeable battery technologies: the odyssey for high energy density, J Solid State Electr, 21 (2017) 1939-1964.

[42] G. Girishkumar, B. McCloskey, A.C. Luntz, S. Swanson, W. Wilcke, Lithium - Air Battery: Promise and Challenges, J Phys Chem Lett, 1 (2010) 2193-2203.

[43] Z.L. Wang, D. Xu, J.J. Xu, X.B. Zhang, Oxygen electrocatalysts in metal-air batteries: from aqueous to nonaqueous electrolytes, Chem Soc Rev, 43 (2014) 7746-7786.

[44] R.M. Dell, Aqueous electrolyte batteries, Philos T R Soc A, 354 (1996) 1515-1527.

[45] A.R. Mainar, E. Iruin, L.C. Colmenares, A. Kvasha, I. de Meatza, M. Bengoechea, O. Leonet, I. Boyano, Z.C. Zhang, J.A. Blazquez, An overview of progress in electrolytes for secondary zinc-air batteries and other storage systems based on zinc, J Energy Storage, 15 (2018) 304-328.

[46] J.O.G. Posada, A.J.R. Rennie, S.P. Villar, V.L. Martins, J. Marinaccio, A. Barnes, C.F. Glover, D.A. Worsley, P.J. Hall, Aqueous batteries as grid scale energy storage solutions, Renew Sust Energ Rev, 68 (2017) 1174-1182.

[47] F. Beck, P. Ruetschi, Rechargeable batteries with aqueous electrolytes, Electrochim Acta, 45 (2000) 2467-2482.

[48] J.B. Goodenough, K.S. Park, The Li-Ion Rechargeable Battery: A Perspective, J Am Chem Soc, 135 (2013) 1167-1176.

[49] N. Nitta, F.X. Wu, J.T. Lee, G. Yushin, Li-ion battery materials: present and future, Mater Today, 18 (2015) 252-264.

[50] N.J. Fisher Scientific, Material Safety Data Sheet, 1,2-Dimethoxyethane, in, 2018.

[51] N.J. Fisher Scientific, Material Safety Data Sheet , Diethyl Carbonate, in, 2018.

[52] N.J. Fisher Scientific, Material Safety Data Sheet, Dimethyl Carbonate, in, 2018.

[53] N.J. Fisher Scientific, Material Safety Data Sheet, Propylene Carbonate, in, 2018.

[54] L.M. Ödkvist, C. Möller, K.-Å. Thuomas, Otoneurologic disturbances caused by solvent pollution, Otolaryngology—Head and Neck Surgery, 106 (1992) 687-692.

[55] A. Fuente, B. McPherson, Organic solvents and hearing loss: The challenge for audiology, Int J Audiol, 45 (2006) 367-381.

[56] W.J. Sułkowski, S. Kowalska, W. Matyja, W. Guzek, W. Wesołowski, W. Szymczak, P. Kostrzewski, Effects of occupational exposure to a mixture of solvents on the inner ear: a field study, Int J Occup Med Environ Health, 15 (2002) 247-256.

[57] L. Hodgkinson, D. Prasher, Effects of industrial solvents on hearing and balance: a review, Noise and health, 8 (2006) 114.

[58] M. Cowie, Watts, H., Diffusion of Methane and Chloromethanes in Air, Canadian Journal of Chemistry, 49 (1971) 74-77.

[59] J.M. Pommersheim, Ranck, B. A., Measurement of Gaseous Diffusion Coefficients Using the Stefan Cell, Industrial & Engineering Chemistry Fundamentals, 12 (1973) 246-250.

[60] Y. Guo, M.G. He, Q. Zhong, Y. Zhang, Mass Diffusion Coefficients of Dimethyl Carbonate in Heptane and in Air at T = (278.15 to 338.15) K, J Chem Eng Data, 53 (2008) 2861-2864.

[61] T. Funazukuri, C.Y. Kong, S. Kagei, Binary diffusion coefficients of acetone in carbon dioxide at 308.2 and 313.2 K in the pressure range from 7.9 to 40 MPa, Int J Thermophys, 21 (2000) 651-669.

[62] L.C. Sun, W.D. Meng, X.Y. Pu, New method to measure liquid diffusivity by analyzing an instantaneous diffusion image, Opt Express, 23 (2015) 23155-23166.

[63] J. Mitrovic, Josef Stefan and his evaporation-diffusion tube-the Stefan diffusion problem, Chem Eng Sci, 75 (2012) 279-281.

[64] E.L. Cussler, Diffusion Mass Transfer in Fluid Systems 3rd Ed., Cambridge University Press, 2009.

[65] R.B. Bird, W.E. Stewart, E.N. Lightfoot, Transport phenomena (Revised 2nd ed.), John Wiley & Sons, 2007.

[66] C.Y. Lee, C.R. Wilke, Measurements of Vapor Diffusion Coefficient, Ind Eng Chem, 46 (1954) 2381-2387.

[67] N.H. Chen, D.F. Othmer, New Generalized Equation for Gas Diffusion Coefficient, J Chem Eng Data, 7 (1962) 37-41.

[68] G.A. Lugg, Diffusion Coefficients of Some Organic and Other Vapors in Air, Anal Chem, 40 (1968) 1072-1077.

[69] R.B. Montgomery, Viscosity and Thermal Conductivity of Air and Diffusivity of Water Vapor in Air, J Meteorol, 4 (1947) 193-196.

[70] 1,2-Dimethoxyethane, in, PubChem, National Institutes of Health. https://pubchem.ncbi.nlm.nih.gov/source/hsdb/73#section=Solubility.

[71] Dimethyl Carbonate, in, Chemical Book. https://www.chemicalbook.com/ChemicalProductProperty_EN_CB8853983.htm.

[72] N.G.C. Astrath, J. Shen, D.T. Song, J.H. Rohling, F.B.G. Astrath, J.Q. Zhou, T. Navessin, Z.S. Liu, C.K.E. Gu, X.S. Zhao, The Effect of Relative Humidity on Binary Gas Diffusion, J Phys Chem B, 113 (2009) 8369-8374.

[73] R.R. Mitchell, B.M. Gallant, C.V. Thompson, Y. Shao-Horn, All-carbon-nanofiber electrodes for high-energy rechargeable Li-O-2 batteries, Energ Environ Sci, 4 (2011) 2952-2958.

[74] M.H. Daneshpajooh, E.A. Mason, E.H. Bresler, R.P. Wendt, Equations for Membrane-Transport - Experimental and Theoretical - Tests of Frictional Model, Biophys J, 15 (1975) 591-613.

[75] S.W. Webb, Gas-Phase Diffusion in Porous Media - Evaluation of an Advective-Dispersive Formulation and the Dusty-Gas Model Including Comparison to Data for Binary Mixtures, in, Sandia, 1996.

[76] D.M. Tartakovsky, M. Dentz, Diffusion in Porous Media: Phenomena and Mechanisms, Transport Porous Med, 130 (2019) 105-127.

[77] L. Pisani, Multi-component gas mixture diffusion through porous media: A 1D analytical solution, Int J Heat Mass Tran, 51 (2008) 650-660.

[78] R. O'hayre, S.-W. Cha, W. Colella, F.B. Prinz, Fuel cell fundamentals, John Wiley & Sons, 2016.

[79] Thermal resistance, in, nuclear-power.net https://www.nuclear-power.net/nuclear-engineering/heat-transfer/thermal-conduction/thermal-resistance-thermal-resistivity/

[80] N.P. Lebedeva, L. Boon-Brett, Considerations on the Chemical Toxicity of Contemporary Li-Ion Battery Electrolytes and Their Components, J Electrochem Soc, 163 (2016) A821-A830.